A Path-Based Switch Open Circuit Fault-Tolerant Method for Three-Phase DAB Converter

Yuanpeng Guan, Yiting Xiao, Li Qin, Xiong Liu, *Senior Member, IEEE*, Hui Deng, and Weixiong Wu

***Abstract*—The three-phase dual active bridge (DAB3) converter achieves the bidirectional power transmission and voltage conversion in dc power grid. However, DAB3 is susceptible to switch open circuit fault (SOCF), causing transmission power loss and excessive current stress. Thus, a path-based fault-tolerant method (PFTM) for SOCF in DAB3 is proposed. First, the transferred energy of each phase is investigated by modality analysis of DAB3, thus, a path energization method is proposed for PFTM, and switching pattern reconfiguration strategy is summarized by switching functions during SOCF, enlarging maximum transmission power within maximum high-frequency-link (HFL) inductor current. Moreover, in the PFTM, the fault paths/legs are employed, reconfiguring the current path of modality, actively adjusting the ON-time of antiparallel diode, and realizing the bidirectional transmission power improvement. Furthermore, the optimization strategy of phase shift ratio is proposed to reduce HFL current stress and keep zero-voltage switching, when SOCF is in primary and secondary sides. Compared with traditional methods, the PFTM can realize a wider power range and voltage gain, and a higher maximum transmission power, to ensure the safety and reliability of DAB3. Finally, experimental results verify the theoretical analysis.**

***Index Terms*—Maximum transmission power, path-based fault-tolerant method (PFTM), switch open circuit fault (SOCF), three-phase dual active bridge (DAB3) converter.**

NOMENCLATURE

DAB3	Three-phase dual active bridge dc–dc converter.
HFL	High-frequency-link.
SOCF	Switch open circuit fault.
ZVS	Zero-voltage switching.
PFTM	Path-based fault-tolerant method.
D_i	Antiparallel diodes of MOSFETs, $i = 1 \ldots 12$.
D	Outer phase shift ratio.
d_1	Phase shift ratio between phases A and B.
d_2	Phase shift ratio between phases B and C.
E_i	Fault modality that occurs after SOCF, $i = 1 \ldots 10$.
f_s	Switching frequency.
i_p	Input current.
i_s	Output current.
i_x	Three-phase high-frequency-link current, $x =$ A, B, C.
$I_{\max}$	Maximum value of three-phase high-frequency-link current.
k	Voltage gain.
L_x	Equivalent high-frequency-link inductor, $x =$ A, B, C.
L	Equivalent value of high-frequency-link inductor.
m_x	High-frequency-link current slope, $x =$ A, B, C.
n	Turns ratio of transformer.
N_i	Modality in normal operation, $i = 1 \ldots 18$.
P	Transmission power in PFTM.
P_{nom}	Transmission power in normal.
P_{op}	Transmission power in open-phase method.
P_{fr}	Transmission power in frozen-fault-leg method.
$P_{\max}$	Maximum value of P.
S_i	MOSFETs, $i = 1 \ldots 12$.
S_x	Switching function, $x =$ A, B, C, a, b, c.
T	One period.
T_{hs}	Half-period.
$\mathrm{T}_{\mathrm{P}i}$	New modality when PFTM is employed for primary SOCF, $i = 1 \ldots 6$.
$\mathrm{T}_{\mathrm{S}i}$	New modality when PFTM is employed for secondary SOCF, $i = 1 \ldots 2$.
V_1	Input voltage.
V_2	Output voltage.
V_{xN}	Three-phase voltage of the primary side, $x =$ A, B, C.
V_{xM}	Three-phase voltage of the secondary side, $x =$ a, b, c.
W_x	Transferred energy of each phase, $x =$ A, B, C, a, b, c.
W	Total transferred energy.
W_{nom}	Total transferred energy in normal.
W_x'	Transferred energy of each phase in PFTM, $x =$ A, B, C, a, b, c.
W'	Total transferred energy in PFTM.

Manuscript received 27 May 2023; revised 13 August 2023; accepted 8 September 2023. Date of publication 18 September 2023; date of current version 6 December 2023. This work was supported in part by the Natural Science Foundation of Guangdong Province under Grants 2021A1515110014 and 2020A1515110547, in part by the National Natural Science Foundation of China under Grant 62301168, and in part by the Science and Technology Project of China Southern Power Grid under Grant GDKJXM20230246 (030100KC23020017). Recommended for publication by Associate Editor A. Marques Cardoso. *(Corresponding author: Hui Deng.)*

Yuanpeng Guan is with the School of Automation, Guangdong University of Technology, Guangzhou 510006, China (e-mail: guanyuanpeng@126.com).

Yiting Xiao, Xiong Liu, Hui Deng, and Weixiong Wu are with the Energy Electricity Research Center, Jinan University, Zhuhai 519070, China (e-mail: xiaoyt@stu2021.jnu.edu.cn; liushawn123@ieee.org; dengh@jnu.edu.cn; weixiongw@126.com).

Li Qin is with the School of Electrical Engineering, Guangxi University, Nanning 530004, China (e-mail: qinli@st.gxu.edu.cn).

Color versions of one or more figures in this article are available at https://doi.org/10.1109/TPEL.2023.3316265.

Digital Object Identifier 10.1109/TPEL.2023.3316265

$W_{\text{Si-}nom}$ Transferred energy of each switch in normal, $i = 1 \ldots 12$.
$W_{\text{Si-SOCF}}$ Transferred energy of each switch in SOCF, $i = 1 \ldots 12$.
W'_{Si} Transferred energy of each switch in PFTM, $i = 1 \ldots 12$.

I. Introduction

In RECENT years, the three-phase dual active bridge (DAB3) converter has been widely used in dc power grid, due to its high directional power transmission and efficient dc voltage transformation [1], [2]. However, the switch is one of the vulnerable components in power electronics converter, and switch fault accounts for about 46% of the total faults [3]. The switch open circuit fault (SOCF) is significant in DAB3, leading to component overstress, transformer saturation, and transmission power loss [4], [5]. Therefore, reducing SOCF impact is necessary to keep the stability and reliability of DAB3 and dc power grid [6], [7].

To maintain the safe operation of the system after SOCF, the common methods are fault isolation and fault tolerance. In the fault isolation method, when SOCF occurs, the fault submodule is blocked by turning OFF all switches in the fault submodule, and the other submodules remain in normal operation [8]. This method isolates the fault submodule, preventing fault impact on whole system. It is usually employed for multiple modular converters. However, for the SOCF in the single modular converter, the system will be interrupted, and the component overstress, transformer saturation, and transmission power loss will be exacerbated [9].

Therefore, to withstand SOCF and improve the reliability of DAB3, several fault-tolerant methods have been proposed. The previous fault-tolerant methods for DAB-type converters mainly contain the following categories.

1) Redundant hardware [10], [11], [12]. The redundant hardware is used to compensate the failure state in SOCF, including redundant switch, bridge leg, and module. In [10], a redundant switch is used to maintain the power transmission for series-resonant dc–dc converter under fault operation. In [11], the redundant bridge leg and inductor are applied to replace the fault leg for the three-phase full-bridge circuits in the dual-winding motor drive system, guaranteeing the drive system to work normally. In [12], the redundant bridge leg is applied to isolate fault bridge leg for the proposed three-level T-type inverter, maintaining the normal output. The topologies in [11] and [12] can be a form of three-phase full-bridge in DAB3. Thus, the redundant bridge leg method provides a way for SOCF tolerance in DAB3. However, these redundant hardware methods make topology more complex and have a high cost of redundancy, which is not suitable for DAB3 with at least 12 switches.
2) Topology modification [13], [14]. In [13], a fault-tolerant capacitor leg is employed, and the complementary switch in the faulty leg is shorted and in DAB. In [14], the topology of DAB is reconfigured by a half-bridge conduction branch after fault, which maintains power transmission. However, this method makes topology more complex, which is not suitable for DAB3 with the Y-Y connection.
3) Modulation reconstruction [15], [16], [17], [18], [19], [20], [21]. The switch state is reconstructed to maintain the operation of the converter in SOCF, without complex control strategies and high-cost redundancy. In [15], when SOCF occurs in secondary side, the fault leg is frozen to obtain symmetrical topology, eliminating the dc bias and maintaining stable operation for DAB. In [16], the fault complementary switch or the fault leg is blocked to reconfigure the symmetric topology, eliminating the dc bias and voltage imbalance in 2/3-level DAB during SOCF. In [17], the fault leg of DAB3 is frozen in secondary SOCF. In the frozen-fault-leg method, the antiparallel diode is employed to reconfigure topology after SOCF, making the waveforms of high-frequency-link (HFL) voltage symmetrical. However, in the frozen-fault-leg method, the impacts of the specific modality and its duration on the performance are usually ignored during operation, causing the transmission power in fault-tolerant operation is reduced greatly. Moreover, the current path is limited and reduced. Then, the transmission power is reduced, especially the transmission power from the fault primary side to the normal secondary side. Thus, the frozen-fault-leg method is not suitable for primary SOCF. In [18] and [19], a primary side lower power method is proposed for primary SOCF of DAB. However, there is a dc bias in the transformer current, leading to transformer saturation. Besides, the reduced current stress and improved transmission power are contradictory in SOCF. The open-phase method is applied for DAB3 within Y-Δ connection [20] and current-fed DAB3 [21] during SOCF, which makes DAB3 operate in single-phase mode. However, DAB3 transfers at most two-thirds of the normal power by this method in SOCF, which greatly reduces transmission power.

Therefore, in the conventional SOCF tolerant methods for DAB3, the transmission power is limited and the current stress is increased. It has negative impacts on the performance of system and needs to be improved.

To solve the above-mentioned issues, a path-based fault-tolerant method (PFTM) for DAB3 in SOCF is proposed in this article, to improve bidirectional transmission power, reduce current stress, and keep zero-voltage switching (ZVS). First, based on modality and path analysis during SOCF in DAB3, a path energization method is proposed to reveal the relationship between the switching pattern and transferred energy. Then, the switching pattern reconfiguration strategy is summarized by switching functions during SOCF, to enlarge the maximum transmission power within the maximum HFL inductor current. Second, PFTM is proposed for SOCF tolerance on primary and secondary sides. In the PFTM, fault paths/legs are employed to reconfigure current path of modality, actively adjusting the ON-time of antiparallel diode, enlarging bidirectional transmission power within maximum HFL inductor current. Third, based on the fault-tolerant operation and bidirectional transmission power

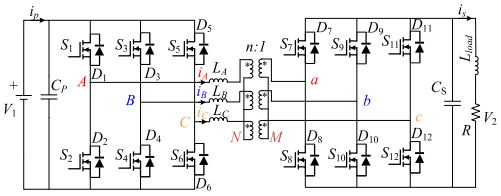

Fig. 1. Topology of DAB3 based on Y-Y connection.

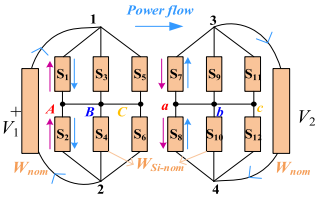

Fig. 2. Transferred energy in normal operation.

improvement, the optimization strategy of phase shift ratio is proposed to reduce HFL current stress and keep ZVS. Moreover, compared with traditional methods, the PFTM can realize a wider power range and voltage gain, and a higher bidirectional transmission power, keeping ZVS.

The rest of this article is organized as follows. In Section II, the normal and SOCF operation of DAB3 are depicted and the path energization method is proposed for PFTM. In Section III, the PFTM is introduced and the operating principle is detailed. In Section IV, the performances of DAB3 under PFTM are analyzed. In Section V, experiments are performed to verify theoretical analyses. Section VI concludes this article.

II. Normal and SOCF Operations of DAB3

A. Normal Operation

The topology of DAB3 based on Y-Y connection is shown in Fig. 1. In the primary side of DAB3, the phases are represented by "phase A," "phase B," and "phase C," respectively. In the secondary side of DAB3, the phases are represented by "phase a," "phase b," and "phase c," respectively. Phase a (b, c) is the dotted phase of phase A (B, C), and phase A (B, C) is the dotted phase of phase a (b, c). V_1 and V_2 are input and output dc voltages. i_p and i_s are input and output dc currents. C_P and C_S are capacitances on primary and secondary sides. Switches S_1–S_6 with antiparallel diodes D_1–D_6 are in primary three-phase bridge, and S_7–S_{12} with antiparallel diodes D_7–D_{12} are in secondary three-phase bridge. The turns ratio of high frequency transformer is n:1, and the star points are denoted as N in primary side and M in secondary side. L_A, L_B, and L_C are the equivalent transformer inductors, and $L_A = L_B = L_C \approx L$. i_A, i_B, and i_C represent the three-phase HFL currents, respectively.

The switching frequency is defined as f_s. T is one period and T_{hs} is half-period. D is outer phase shift ratio, and set as [0, 1]; d_1 is phase shift ratio between phases A and B, d_2 is phase shift ratio between phases B and C, phase shift ratio between phases C and A is (2-d_1-d_2), and $d_1 = d_2$.

The three-phase HFL currents can be described as follows:

$$i_{A,B,C}(t) = I_{A0,B0,C0} + \frac{V_{AN,BN,CN}(t) - nV_{aM,bM,cM}(t)}{L} \cdot \Delta t \quad (1)$$

where I_{A0}, I_{B0}, and I_{C0} are the initial current in each time interval, and Δt is the duration of an interval. V_{AN}, V_{BN}, and V_{CN} are the phase voltage of primary side. V_{aM}, V_{bM}, and V_{cM} are the phase voltage of secondary side. The phase voltages can be described by switching function S_x (x = A, B, C, a, b, c)

$$\begin{cases} V_{AN,BN,CN}(t) = (2S_{A,B,C} - S_{B,C,A} - S_{C,A,B})V_1/3 \\ V_{aM,bM,cM}(t) = (2S_{a,b,c} - S_{b,c,a} - S_{c,a,b})V_2/3 \end{cases} \quad (2)$$

where $S_x = 1$ represents the path related to positive potential in phase x is conductive. $S_x = 0$ represents the path related to negative potential in phase x is conductive. In normal operation, if $S_x = 1$, the upper switch/diode is ON and the lower switch/diode is OFF in path. If $S_x = 0$, the upper switch/diode is OFF and the lower switch/diode is ON in path. In SOCF operation, the upper switch and lower switch are the conditions in fault. When the upper switch is SOCF, if $S_x = 1$, the upper diode is ON and the lower switch/diode is OFF in path. If $S_x = 0$, the upper diode is OFF and the lower switch/diode is ON in path. When the lower switch is SOCF, if $S_x = 1$, the upper switch/diode is ON and the lower diode is OFF in path. If $S_x = 0$, the upper switch/diode is OFF and the lower diode is ON in path. Based on Y-Y connection, the three-phase HFL currents are regarded as balanced [22]

$$i_A(t) + i_B(t) + i_C(t) = 0. \quad (3)$$

Besides, the transferred energy of each phase W_x (x = A, B, C, a, b, c) is described as follows:

$$\begin{cases} W_A = W_a = \int_0^T V_{AN}(t) i_A(t) dt \\ W_B = W_b = \int_0^T V_{BN}(t) i_B(t) dt \\ W_C = W_c = \int_0^T V_{CN}(t) i_C(t) dt \end{cases} \quad (4)$$

where the total transferred energy $W = W_A + W_B + W_C$. Then, the transferred energy is carried out by the switches in the path. Thus, a path energization method can be proposed.

The transferred energy of path can be described by the corresponding current slope. Based on (1) and (2), the HFL current slope m_x (x = A, B, C, a, b, c) can be expressed as follows:

$$\begin{cases} m_A = m_a \\ \quad = |(2S_A - 2kS_a) + (2kS_b + 2kS_c - S_B - S_C)|\, V_1/3L \\ m_B = m_b \\ = |(2S_B - 2kS_b) + (2kS_a + 2kS_c - S_A - S_C)|\, V_1/3L \\ m_C = m_c \\ \quad = |(2S_C - 2kS_c) + (2kS_b + 2kS_a - S_B - S_A)|\, V_1/3L \end{cases} \quad (5)$$

where $k = nV_2/V_1$. m_x is mainly determined by the switch states, so m_x can be adjusted by switching pattern reconfiguration.

According to the proposed path energization method, in Fig. 2, the power flow from the primary side to the secondary side represents the forward power flow. Besides, the path through switch represents the forward direction, and path through antiparallel

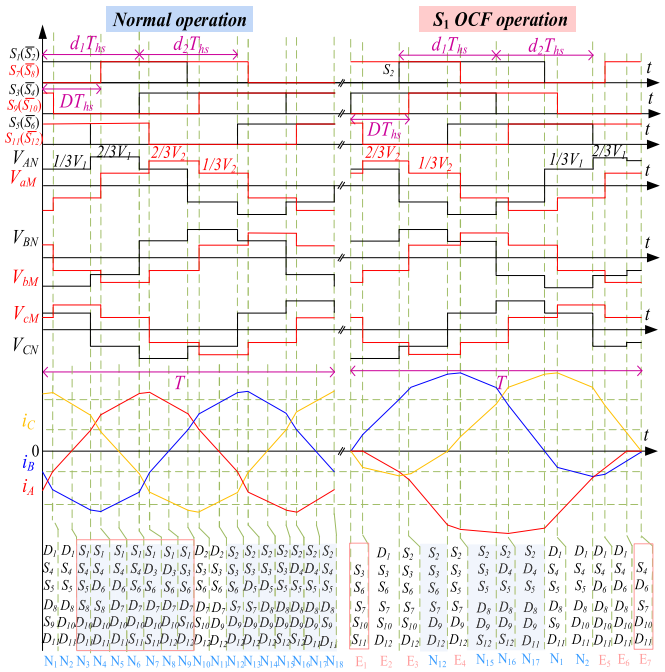

Fig. 3. Waveforms of DAB3 when S_1 is SOCF.

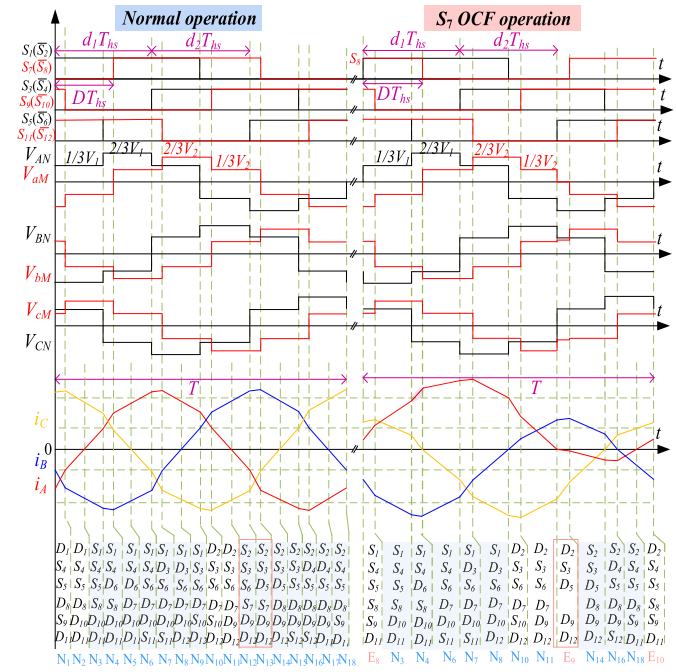

Fig. 5. Waveforms of DAB3 when S_7 is SOCF.

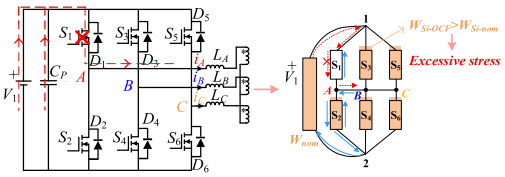

Fig. 4. Path and transferred energy of DAB3 when S_1 is SOCF.

diode represents the reverse direction. But both conducting switch and diode are represented by 0 or 1 in the switching function S_x. For example, the direction from node 1 to A represents the path of S_1-ON, and the direction from node A to 1 represents the path of D_1-ON. But both the path of S_1-ON and the path of D_1-ON are represented by switching function $S_A = 1$. In normal, each switch is used equally in path to transfer energy bidirectionally. The transferred energy of each switch is $W_{Si\text{-}nom}$ in normal.

The waveforms and modal paths of DAB3 in normal operation are shown on the left side of Fig. 3 and 5, where N_1–N_{18} are the normal modalities. The modal path is the current path in each modality, which is listed below the waveforms. In normal operation, the current and voltage waveforms of each phase are the same, the phase shift time between each phase is $2/3T_{hs}$, and current waveforms are symmetric without dc bias. Thus, the transferred energy of each phase is equal to 1/3 of the total energy W_{nom}. Then, the transmission power P_{nom} of DAB3 is [6]

$$P_{nom} = \frac{W_{nom}}{T} = \begin{cases} \frac{nV_1V_2}{2f_sL}D(\frac{2}{3} - \frac{D}{2}) & 0 \le D \le \frac{1}{3} \\ \frac{nV_1V_2}{2f_sL}(D - D^2 - \frac{1}{18}) & \frac{1}{3} \le D \le \frac{2}{3} \end{cases} \tag{6}$$

TABLE I
TRANSFERRED ENERGY PATHS FROM PRIMARY SIDE TO SECONDARY SIDE IN PHASE A

i_A	i_B	i_C	Current paths	
			Primary side	Secondary side
>0	>0	<0	$S_1S_3S_6$	$D_7S_{10}D_{12}$, $D_7D_9D_{12}$, $S_8D_9D_{12}$
>0	<0	>0	$S_1S_4S_5$, $S_1S_4D_6$	$D_7D_{10}S_{12}$, $D_7D_{10}D_{11}$, $S_8D_{10}D_{11}$
>0	<0	<0	$S_1S_4S_6$, $S_1S_4D_5$, $S_1D_3S_6$	$D_7S_9D_{12}$, $D_7D_{10}D_{12}$, $D_7D_{10}S_{11}$
<0	>0	<0	$S_2S_3S_6$, $S_2S_3D_5$	$D_8D_9S_{11}$, $D_8D_9D_{12}$, $S_7D_9D_{12}$
<0	<0	>0	$S_2S_4S_5$, $S_2D_3S_5$	$D_8S_9D_{11}$, $D_8D_{10}D_{11}$, $S_7D_{10}D_{11}$
<0	>0	>0	$S_2S_3S_5$, $S_2S_3D_6$, $S_2D_4S_5$	$D_8S_{10}D_{11}$, $D_8D_9S_{12}$, $D_8D_9D_{11}$

where P_{nom} is adjusted by D. Moreover, the transferred energy paths from the primary side to the secondary side in phase A are listed in Table I.

From Table I, the conducting primary side switches associated with paths are more than secondary side switches. Thus, the primary side switch is dominant for energy transformation, and the impact of SOCF on primary side is more serious than that on secondary side.

B. Primary Side SOCF

The waveforms and modal paths of DAB3 are shown in Fig. 3, when S_1 of phase A is SOCF. In Fig. 4, there is no feasible path for positive current in fault phase A. Then, the fault modalities E_1–E_7 occur when S_1 is SOCF, and the primary phase voltage in E_1 and E_7 is established as follows:

$$\begin{cases} V_{AN}(t) = (-S_B - S_C)V_1/3 \\ V_{BN}(t) = (2S_B - S_C)V_1/3 \\ V_{CN}(t) = (2S_C - S_B)V_1/3 \end{cases}. \tag{7}$$

Then, the dc bias is accumulated in HFL current by (1) and (7). Thus, a completely negative dc bias occurs in i_A, and i_B and

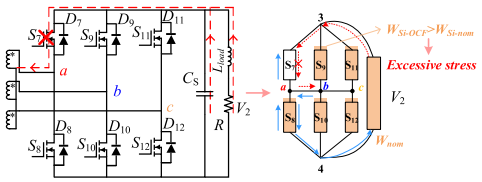

Fig. 6. Path and transferred energy of DAB3 when S_7 is SOCF.

i_C present the positive dc bias to maintain three-phase balance in HFL transformer. It causes excessive current stress and even leads to transformer saturation. Moreover, in the paths of the fault modalities E_1–E_4 in Fig. 3, the current is through the switch directly without freewheeling diode. Thus, the ZVS of S_2, S_3, S_5, and S_7 is destroyed. Besides, in Fig. 4, the fault switch S_1 cannot transmit energy bidirectionally, so transferred energy is maintained at $1/3W_{nom}$ via the rest switches. Then, the transferred energy of each switch $W_{Si\text{-}SOCF}$ in SOCF is larger than $W_{Si\text{-}nom}$ in normal, resulting in normal switch overcurrent.

C. Secondary Side SOCF

The waveforms and modal paths of DAB3 are shown in Fig. 5, when S_7 of phase a is SOCF. In Fig. 6, there is no feasible path for negative current in fault phase a of modalities N_{12} and N_{13}. Then, the fault modalities E_8–E_{10} occur when S_7 is SOCF, and the secondary phase voltage in E_9 is established as follows:

$$\begin{cases} V_{aM}(t) = (-S_b - S_c)V_2/3 \\ V_{bM}(t) = (2S_b - S_c)V_2/3 \\ V_{cM}(t) = (2S_c - S_b)V_2/3 \end{cases}. \tag{8}$$

Then, the dc bias is accumulated in HFL current by (1) and (8), and the fault modality E_9 occurs. Thus, a positive dc bias occurs in i_A, and i_B and i_C present the positive dc bias to maintain three-phase balance in HFL transformer. It causes excessive current stress and even causes saturation of transformers to saturate. Moreover, in the path of the fault modalities E_8 in Fig. 5, the current is through the switch directly without freewheeling diode. Thus, the ZVS of S_1 is destroyed. Similarly, in Fig. 6, the fault switch S_7 cannot transmit energy bidirectionally, so transferred energy is maintained via the rest switches, causing normal switch overcurrent.

Thus, to reduce excessive current stress in SOCF, the total transferred energy should be lower than normal. Moreover, the transferred energy can be lowered by reducing the current slope m_x and adjusting duration. Therefore, the switching pattern reconfiguration strategy is summarized by switching functions to determine HFL current slope m_x during SOCF, as listed in Table II. Then, it achieves transferred power improvement within maximum HFL inductor current by limiting the transferred energy of fault phase, when SOCF occurs. For example, when S_1 is SOCF, the HFL current slope m_A of fault phase A needs to be lowered to limit the transferred energy of fault phase A. As shown in Fig. 3, the negative dc bias is accumulated in HFL current of fault phase A, so V_{AN}(t)-nV_{aM}(t) in fault modalities is lower than 0. Thus, to lower m_A, V_{AN}(t) needs to be increased or

TABLE II
PROPOSED SWITCHING PATTERN RECONFIGURATION STRATEGY IN SOCF

Fault switch	i_A	i_B	i_C	Path (switch functions)
S_1/S_8	-	+	+	$S_A = 1$ *or* $S_a = 0$
S_2/S_7	+	-	-	$S_A = 0$ *or* $S_a = 1$
S_3/S_{10}	+	-	-	$S_B = 0$ *or* $S_b = 1$
S_4/S_9	-	+	+	$S_B = 1$ *or* $S_b = 0$
S_5/S_{12}	+	-	-	$S_C = 0$ *or* $S_c = 1$
S_6/S_{11}	-	+	+	$S_C = 1$ *or* $S_c = 0$

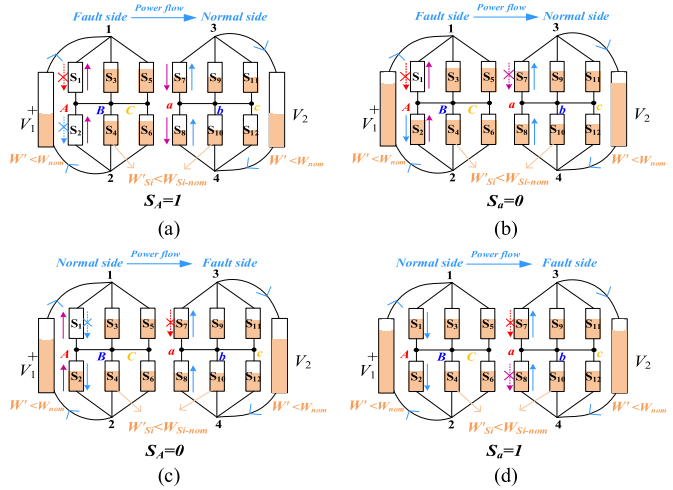

Fig. 7. Proposed switching pattern reconfiguration cases for SOCF. (a) and (b) When S_1 is SOCF. (c) and (d) When S_7 is SOCF.

V_{aM}(t) needs to be lowered. Then, when S_1 is SOCF, switching function $S_a = 0$ is adopted to make V_{aM}(t) lower, or switching function $S_A = 1$ is adopted to make V_{AN}(t) larger. In addition, $S_A = 1$ and $S_a = 0$ are not contradictory and can be satisfied simultaneously or arbitrarily.

When S_1 is SOCF, the employments of "$S_A = 1$" or "$S_a = 0$" are in Fig. 7(a) and (b). The path of D_1-ON and S_2/D_2-OFF or the path of S_7/D_7-OFF and S_8/D_8-ON is employed for fault tolerance. When S_7 is SOCF, the employments of "$S_A = 0$" or "$S_a = 1$" are in Fig. 7(c) and (d). The path of S_1/D_1-OFF and S_2/D_2-ON or the path of D_7-ON and S_8/D_8-OFF is employed for fault tolerance.

III. PFTM FOR SOCF IN PRIMARY AND SECONDARY SIDES OF DAB3 BASED ON PATH ENERGIZATION

A. Primary Side SOCF Tolerance

When SOCF occurs in primary side, the stress and bias of HFL current are excessive without limiting the transmission power. Thus, the PFTM is introduced, including the reconstruction of path and its duration, to achieve tolerant operation, reduce current stress, and improve transmission power. When PFTM is applied for SOCF in primary side, according to Table II, the diode of the dotted phase in normal bridge is employed by blocking the corresponding switches in the dotted phase of the fault phase. Thus, it can achieve tolerant operation for SOCF and ensure that power can be transferred from primary side to secondary side. Furthermore, according to path energization

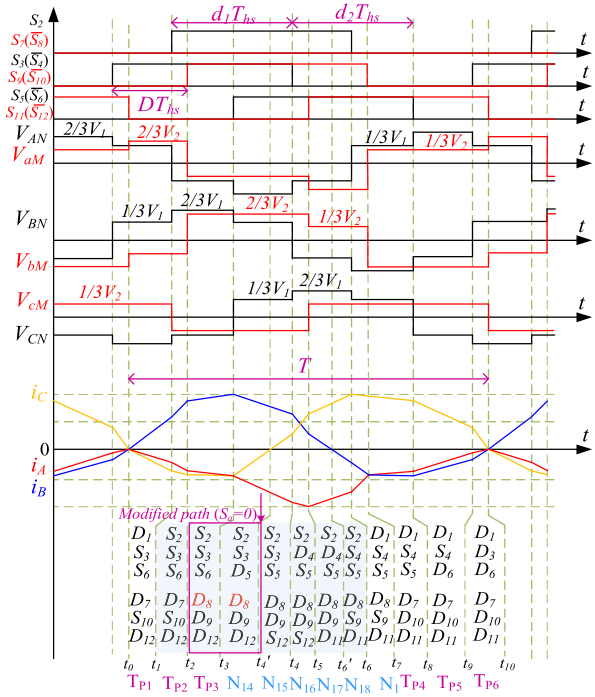

Fig. 8. Waveforms of DAB3 under PFTM when SOCF occurs in S_1.

method, the fault leg is used to reconfigure the current path of modality, actively adjusting the ON-time of antiparallel diode, enlarging the transmission power from the fault side to the normal side. Moreover, to reduce the HFL current stress under maximum HFL current in normal, the HFL current slope can be adjusted by active modulation of fault legs/paths. Meanwhile, the ZVS of switches can be achieved by the direction of HFL current path and switch states. Then, the phase shift ratios d_1 and d_2 are optimal, under transmission power improvement in PFTM and avoiding current overstress during fault-tolerant operation. The duration of the rest of normal switches is maintained as T_{hs}. Thus, in the PFTM, HFL current stress and bidirectional transmission power are optimized in the fault-tolerant operation of DAB3.

For example, when S_1 of the fault phase A is SOCF, the waveforms and modal paths of DAB3 under PFTM are shown in Fig. 8, and T_{P1}–T_{P6} are the new modalities in PFTM. The path with $S_a = 0$ is inserted to replace the path with $S_a = 1$ by blocking S_7 and S_8 of phase a. As shown in Fig. 9(a) and (b), i_A flows through D_8 instead of S_7, so modalities T_{P3} and N_{14} occur during t_2-t_4' in Fig. 8, and modalities N_{12} and E_4 in Fig. 3 do not occur in PFTM in Fig. 8.

The HFL currents in T_{P3} and N_{14} in Fig. 8 are established as (9) and (10), respectively.

$$\begin{cases} i_A(t) = I_{A0} + (-V_1 + nV_2)\cdot \Delta t/3L \\ i_B(t) = I_{B0} + (2V_1 - 2nV_2)\cdot \Delta t/3L \\ i_C(t) = I_{C0} + (-V_1 + nV_2)\cdot \Delta t/3L \end{cases} \tag{9}$$

$$\begin{cases} i_A(t) = I_{A0} + (-2V_1 + nV_2)\cdot \Delta t/3L \\ i_B(t) = I_{B0} + (V_1 - 2nV_2)\cdot \Delta t/3L \\ i_C(t) = I_{C0} + (V_1 + nV_2)\cdot \Delta t/3L \end{cases}. \tag{10}$$

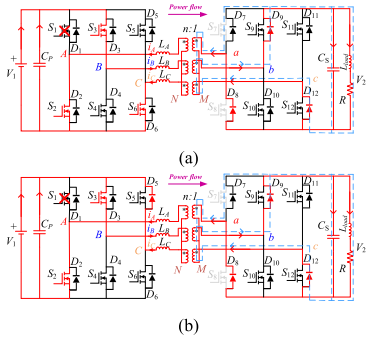

Fig. 9. Modified paths during S_1 in SOCF under PFTM. (a) T_{P3}. (b) N_{14}.

The current i_A in fault phase A is described as follows:

$$\begin{cases} i_A(t_0) = 0 \\ i_A(t_1) = (V_1 - 2nV_2)(2 - D - d_1 - d_2)T_{hs}/3L \\ i_A(t_2) = i_A(t_1) + (-V_1 - 2nV_2)(D + d_1 - 1)T_{hs}/3L \\ i_A(t_3) = i_A(t_2) + (-V_1 + nV_2)(d_2 - D)T_{hs}/3L \\ i_A(t_4) = i_A(t_3) + (-2V_1 + nV_2)(1 - d_2)T_{hs}/3L \\ i_A(t_5) = i_A(t_4) + (-V_1 + nV_2)(D + d_2 - 1)T_{hs}/3L \\ i_A(t_6) = i_A(t_5) + (-V_1 + 2nV_2) \\ \qquad \times (2 - D - d_1 - d_2)T_{hs}/3L \\ i_A(t_7) = i_A(t_6) + (V_1 + 2nV_2)(D + d_1 - 1)T_{hs}/3L \\ i_A(t_8) = i_A(t_7) + (V_1 - nV_2)(d_2 - D)T_{hs}/3L \\ i_A(t_9) = i_A(t_8) + (2V_1 - nV_2)(1 - d_2)T_{hs}/3L \\ i_A(t_{10}) = i_A(t_9) + (V_1 - nV_2)(D + d_2 - 1)T_{hs}/3L \end{cases}. \tag{11}$$

Moreover, based on Table I, the modalities and paths for transferred energy from primary side to secondary side in phase A are marked by blue shade in Fig. 8. According to path energization method, the fault leg is used in T_{P2}-N_{18} to enlarge the transmission power from the fault side to the normal side. Thus, it can achieve tolerant operation for SOCF and ensure transmission power from primary side to secondary side.

Then, D, d_1, and d_2 are changed optimally, and the duration of switches S_1-S_6 and S_9-S_{12} is maintained as T_{hs}. The operation of S_2 in fault leg is optimized, leading to modalities of D_7 and D_8 being changed forcedly. According to (9) and (10), the slopes of i_A, i_B, and i_C are all reduced. Thus, the negative dc bias of i_A and the positive dc bias of i_B and i_C are alleviated, which reduces transferred energy and current stress. So, the HFL current stress is reduced.

Thus, when PFTM is employed for S_1 in SOCF, according to (4) and (9)–(11), the transferred energy W_x' (x = A, B, C, a, b, c) and total energy W' from primary side to secondary side are as follows:

$$\begin{cases} W'_A = W'_a = h\left[\left(\frac{7}{2} - D - 2d_1 - d_2\right)D \right. \\ \qquad \left. + \left(3 - d_1 - \frac{d_2}{2}\right)d_1 + \frac{d_2^2}{4} - \frac{7}{4}\right] \\ W'_B = W'_b = h[(8 - 7D - 2d_1 + 2d_2)D \\ \qquad +(3 - d_1 + d_2)d_1 + (3 - 2d_2)d_2 - 4] \\ W'_C = W'_c = h[(8 - 7D - 2d_1 + 2d_2)D \\ \qquad +(3 - d_1 + d_2)d_1 + (3 - 2d_2)d_2 - 4] \\ W' = 3h\left[(10 - 6D - 4d_1)D + (6 - 2d_1)d_1 \right. \\ \qquad \left. + (2 - d_2)d_2 - 5\right] \end{cases} \tag{12}$$

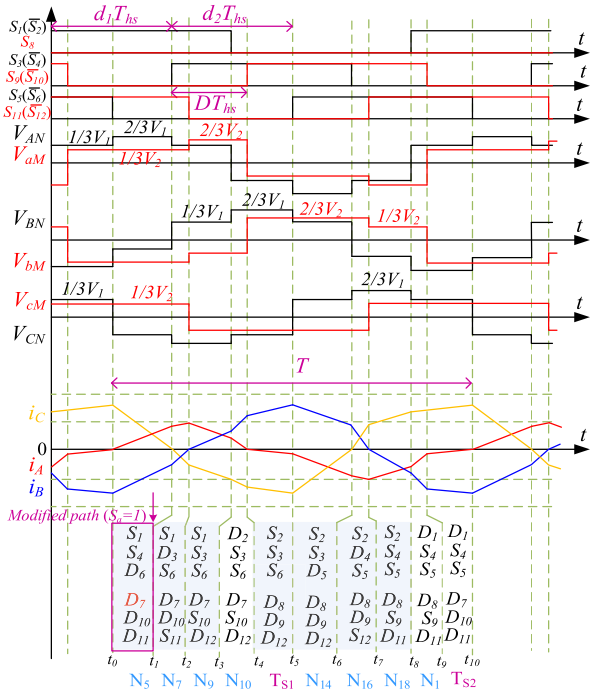

Fig. 10. Waveforms of DAB3 under PFTM when SOCF occurs in S_7.

where $h = V_1V_2T^2/36L$. In (12), the transferred energy of each phase can be regulated by D, d_1, and d_2, to further reduce current stress and improve transmission power.

B. Secondary Side SOCF Tolerance

When SOCF occurs on secondary side, the stress and bias of HFL current are also excessive without limiting the transmission power. Thus, the PFTM is introduced, including the reconstruction of path and its duration, to achieve tolerant operation, reduce current stress, and improve transmission power. When PFTM is applied for SOCF in secondary side, according to Table II, the diode in the fault phase is employed by blocking complementary switches in the fault phase, to achieve tolerant operation. Furthermore, according to path energization method, the fault path is used to reconfigure the current path of modality, actively adjusting the ON-time of antiparallel diode, ensuring transmission power from normal side to fault side. Moreover, to reduce the HFL current stress under maximum HFL current in normal, the HFL current slope can be adjusted by active modulation of fault legs/paths. Meanwhile, the ZVS of all switches can be achieved by the direction of HFL current path and switch states. Then, the phase shift ratios d_1 and d_2 are optimal, under transmission power improvement in PFTM and avoiding current overstress during fault-tolerant operation. The duration of the rest of normal switches is maintained as T_{hs}. Thus, in the PFTM, the HFL current stress is optimized and the transmission power is maintained, based on fault-tolerant operation of DAB3.

For example, when S_7 of the fault phase a is SOCF, the waveforms and modal paths of DAB3 under PFTM are shown in Fig. 10, and T_{S1}-T_{S2} are the new modalities in PFTM. The

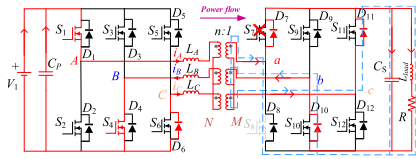

Fig. 11. Modified paths during S_7 in SOCF under PFTM.

path with $S_a = 1$ is inserted to replace the path with $S_a = 0$ by blocking S_8 of phase a. In Fig. 11, i_A flows through D_7 instead of S_8, so the modality N_5 occurs during t_0-t_1 of Fig. 10, and modality N_4 in Fig. 5 does not occur in PFTM in Fig. 10.

The HFL currents in N_5 in Fig. 10 are established as follows:

$$\begin{cases} i_A(t) = I_{A0} + (2V_1 - nV_2)\cdot \Delta t/3L \\ i_B(t) = I_{B0} + (-V_1 + 2nV_2)\cdot \Delta t/3L \\ i_C(t) = I_{C0} + (-V_1 - nV_2)\cdot \Delta t/3L \end{cases} \tag{13}$$

where the slopes of i_A, i_B, and i_C are all reduced. Thus, the positive dc bias of i_A and the negative dc bias of i_B and i_C are alleviated, which reduces transferred energy and current stress.

The i_A in dotted phase A of fault phase a is described as follows:

$$\begin{cases} i_A(t_0) = 0 \\ i_A(t_1) = (2V_1 - nV_2)(1 - d_2)T_{hs}/3L \\ i_A(t_2) = i_A(t_1) + (V_1 - nV_2)(D + d_2 - 1)T_{hs}/3L \\ i_A(t_3) = i_A(t_2) + (V_1 - 2nV_2)(2 - D - d_1 - d_2)T_{hs}/3L \\ i_A(t_4) = i_A(t_3) + (-V_1 - 2nV_2)(D + d_1 - 1)T_{hs}/3L \\ i_A(t_5) = i_A(t_4) + (-V_1 + nV_2)(d_2 - D)T_{hs}/3L \\ i_A(t_6) = i_A(t_5) + (-2V_1 + nV_2)(1 - d_2)T_{hs}/3L \\ i_A(t_7) = i_A(t_6) + (-V_1 + nV_2)(D + d_2 - 1)T_{hs}/3L \\ i_A(t_8) = i_A(t_7) + (-V_1 + 2nV_2) \\ \qquad \times (2 - D - d_1 - d_2)T_{hs}/3L \\ i_A(t_9) = i_A(t_8) + (V_1 + 2nV_2)(D + d_1 - 1)T_{hs}/3L \\ i_A(t_{10}) = i_A(t_9) + (V_1 - nV_2)(d_2 - D)T_{hs}/3L \end{cases} \tag{14}$$

Moreover, based on Table I, the modalities and paths for transferred energy from primary side to secondary side in phase A are marked by blue shade in Fig. 10. According to path energization method, except for N_1, N_{10}, and T_{S2}, the fault paths are used in the rest of modalities to realize the transmission power from the normal side to the fault side. Thus, it can achieve tolerant operation for SOCF and maintain transmission power from primary side to secondary side.

Then, D, d_1, and d_2 are changed optimally, and the duration of switches S_1-S_6 and S_9-S_{12} is maintained as T_{hs}. The operation of S_1 and S_2 in phase A is optimized, leading to modalities of D_7 and D_8 being changed forcedly. According to (13), the slopes of i_A, i_B, and i_C are all reduced. Thus, the positive dc bias of i_A and the negative dc bias of i_B and i_C are alleviated, which reduces transferred energy and current stress. So, the HFL current stress is reduced.

Thus, when PFTM is employed for S_7 in SOCF, according to (4), (13), and (14), the transferred energy W_x' (x = A, B, C, a, b, c) and total energy W' from primary side to secondary side are

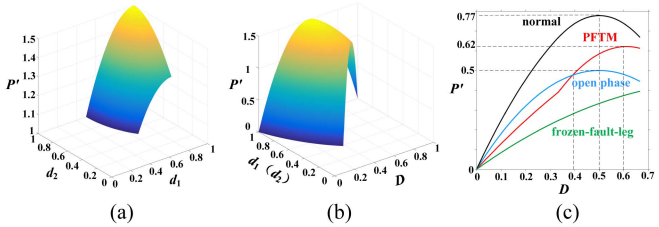

Fig. 12. Transmission power curves. (a) Relationship among transmission power, d_1, and d_2 under PFTM. (b) Relationship among transmission power, $d_1(d_2)$, and D under PFTM. (c) Transmission power comparison among fault-tolerant methods and normal operation.

equal to (12). Thus, the transferred energy of each phase can be regulated by D, d_1, and d_2, to further reduce the current stress and improve transmission power.

In summary, some achievements in PFTM are as follows.

1) Reconfiguring the fault paths/legs via path energization method. It improves the bidirectional power transmission of DAB3 in SOCF via inserting the paths related to normal switch of fault paths/legs, especially the transmission power from fault side to normal side.
2) Optimizing the phase differences between fault phase and normal phase. The operation of normal switch in fault legs/paths is reconfigured in PFTM, optimizing the duration of the corresponding modalities about the antiparallel diodes, whatever SOCF is in primary and secondary sides. The optimal range of phase shift ratios D, d_1, and d_2 is analyzed in Section IV-E. Thus, in PFTM, HFL current stress is reduced.

IV. Performance Analysis of Proposed Fault-Tolerant Method

A. Transmission Power Analysis

Combined with (12), the transmission power in PFTM is summarized as follows:

$$P = W'/T = \frac{nV_1V_2}{12f_sL}[(10-6D-4d_1)D + (6-2d_1)d_1 + (2-d_2)d_2 - 5]. \quad (15)$$

In the traditional open-phase method [23], the transmission power P_{op} of DAB3 is

$$P_{op} = \frac{nV_1V_2}{4f_sL}D(1-D). \quad (16)$$

In the traditional frozen-fault-leg method [17], the transmission power P_{fr} of DAB3 is

$$P_{fr} = \frac{nV_1V_2}{4f_sL}D\left(\frac{24}{27} - \frac{4D}{9}\right). \quad (17)$$

According to (6) and (15)–(17), the transmission power curves are shown in Fig. 12. The unified transmission power P' is defined as $P' = P/P_{base}$ and $P_{base} = nV_1V_2/8f_sL$. When $D = 0.5$, P_{op} achieves maximum $P_{\text{op-max}} = P_{base}$. From Fig. 12(a), for DAB3 under PFTM, the transmission power is with a wider adjustable area and larger than $P_{\text{op-max}}$. When $d_1 = d_2$, the transmission power range of PFTM is shown in Fig. 12(b) and maximum transmission power $P_{\max}$ under PFTM is $P_{\max} = 1.5P_{\text{op-max}}$. When $d_1 = d_2 = 2/3$, the transmission power curve with varied outer phase shift ratio D is shown in Fig. 12(c). In normal, the transmission power achieves maximum $P_{\text{normal-max}}$, when $D = 0.5$. When $D = 0.6$, transmission power under PFTM achieves maximum, 80.5% of $P_{\text{normal-max}}$. Compared with traditional methods, transmission power under PFTM is increased by 24%.

TABLE III
ZVS Conditions of Switch in PFTM

Phase	A	B	C
Primary side SOCF (Fig. 8)			
ZVS conditions of switch	----	S_3: $i_B(t_9)<0$ S_4: $i_B(t_4)>0$ S_9: $i_B(t_2)>0$ S_{10}: $i_B(t_7)<0$	S_5: $i_C(t_3)<0$ S_6: $i_C(t_8)>0$ S_{11}: $i_C(t_5)>0$ S_{12}: $i_C(t_0)<0$
Secondary side SOCF (Fig. 10)			
ZVS conditions of switch	S_1: $i_A(t_8)<0$ S_2: $i_A(t_3)>0$	S_3: $i_B(t_1)<0$ S_4: $i_B(t_6)>0$ S_9: $i_B(t_4)>0$ S_{10}: $i_B(t_9)<0$	S_5: $i_C(t_5)<0$ S_6: $i_C(t_0)>0$ S_{11}: $i_C(t_7)>0$ S_{12}: $i_C(t_2)<0$

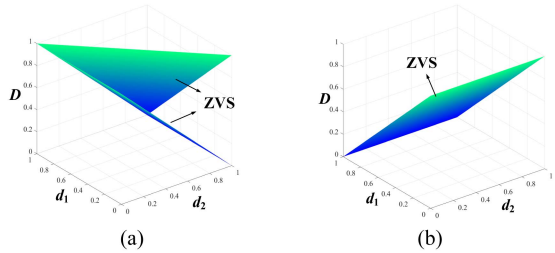

Fig. 13. ZVS ranges of DAB3 under PFTM. (a) SOCF in primary side. (b) SOCF in secondary side.

B. ZVS Range Analysis

The direction of current is considered as the basic condition for ZVS approximately [24]. According to Figs. 8 and 10, the ZVS conditions of switch in PFTM are listed in Table III.

Combined with (11) and Table III, the ZVS condition under primary SOCF is summarized as follows:

$$\begin{cases} D \le 2 - d_1 - d_2 \\ D \ge 1 - d_2 \\ (3d_2 - 1)k + 2D - d_1 + d_2 + 2 \ge 0 \\ [(D + d_1 - 2d_2 - 1)k - D + 2d_1] \le 0 \end{cases}. \quad (18)$$

Combined with (14) and Table III, the ZVS condition under secondary SOCF is summarized as follows:

$$\begin{cases} (k-2)(d_2-1) \ge 0 \\ (D + 2d_1 + 2d_2 - 4)k - d_1 - 2d_2 + 3 \ge 0 \\ (D - 3d_2/2 + 1)k + d_1 + 3d_2/2 - 2 \ge 0 \\ (k-1)(D - d_2) \le 0 \end{cases}. \quad (19)$$

The ZVS ranges of DAB3 under PFTM are displayed in Fig. 13. In primary side SOCF, except for switch in fault leg, the switches can achieve ZVS in PFTM in Fig. 13(a). In secondary side SOCF, all switches can achieve ZVS in PFTM in

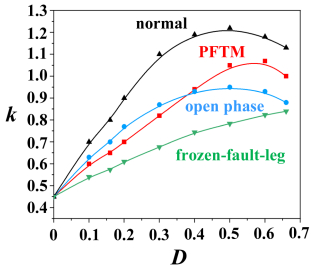

Fig. 14. Voltage gain k of DAB3 with varied phase shift D.

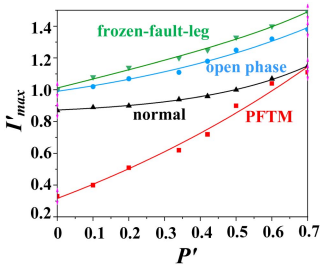

Fig. 15. Current stress in DAB3 with varied load conditions.

Fig. 13(b). However, in traditional methods by frozen-fault-leg and open-phase, the HFL resonant inductor value is increased by changed winding structure [23]. Thus, the HFL current slope is reduced, leading to ZVS loss probably and unexpectedly.

C. Voltage Gain Analysis

According to (18), voltage gain $k = nV_2/V_1$ can be derived as follows:

$$k = \frac{R}{12f_sL} \times [(10 - 6D - 4d_1)D + (6 - 2d_1)d_1 + (2 - d_2)d_2 - 5]. \tag{20}$$

Fig. 14 shows the voltage gain k of DAB3 with varied phase shift D. The voltage gain range of DAB3 under PFTM is from 0.45 to 1.05. Besides, the voltage gain range under PFTM is increased by 20%, compared with the traditional methods.

D. Current Stress Analysis

According to (11), in primary side SOCF, the maximum value of three-phase current I_{max} in PFTM can be described as follows:

$$I_{\max} = |i_A(t_5)| = (2D + 2d_1 + d_2 + 2k - 3kd_2 - 2)V_1/12f_sL. \tag{21}$$

According to (14), in secondary side SOCF, I_{max} in PFTM can be described as follows:

$$I_{\max} = |i_A(t_7)| = [(D - 3d_2 + 2)k + D + 2d_1 + 2d_2 - 3]V_1/12f_sL. \tag{22}$$

The unified maximum current stress I'_{max} is defined as $I'_{max} = I_{max}/I_{base}$, and $I_{base} = V_1/6f_sL$.

The current stress of DAB3 in normal, open-phase, and frozen-fault-leg methods are as follows:

$$\begin{cases} I_{\max-nom} = (3kD + 1)V_1/18f_sL \\ I_{\max-op} = D(1 - D)V_1/4f_sL \\ I_{\max-fr} = DV_1/4f_sL \end{cases}. \tag{23}$$

Based on (21)–(23), the current stress in DAB3 with varied load conditions is shown in Fig. 15. Under SOCF, PFTM can reduce current stress in the full power range, compared with open-phase and frozen-fault-leg methods. Thus, transformer saturation can be avoided, and transformer operates safely.

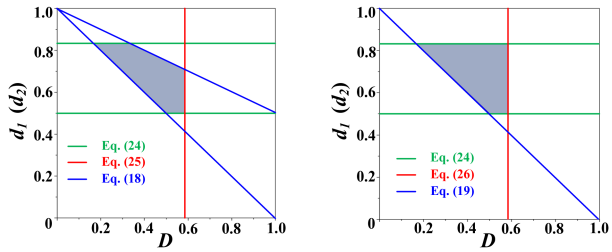

Fig. 16. Optimal range of D, d_1, and d_2. (a) When SOCF occurs on the primary side. (b) When SOCF occurs on the secondary side.

E. Phase Shift Ratio Optimization

As earlier analyses, transmission power, current stress, and ZVS range in PFTM limit the phase shift ratios D, d_1, and d_2, providing the optimization for D, d_1, and d_2 in fault-tolerant operation. The common constraints of D, d_1, and d_2 are

$$\begin{cases} 0 \le D \le 1 \\ 1/2 \le d_1 = d_2 \le 5/6 \end{cases}. \tag{24}$$

When SOCF occurs on the primary side, the current stress I_{max} in PFTM needs to be less than the maximum HFL inductor current $I_{max\text{-}nom}$ in normal to meet the reliability and safe operation, i.e.,

$$I_{\max} < I_{\max-nom} \Rightarrow (2D + 2d_1 + d_2 + 2k - 3kd_2 - 2) V_1/12f_sL \le 0.195kV_1/2f_sL. \tag{25}$$

To keep the ZVS, the constraint of ZVS in PFTM is shown in (18). Combined with (18), (24), and (25), the optimal range of phase shift ratios D and $d_1 = d_2$ are obtained, as in Fig. 16(a).

When SOCF occurs on the secondary side, the current stress I_{max} in PFTM needs to be less than $I_{max\text{-}nom}$ to meet the reliability and safe operation, i.e.,

$$I_{\max} < I_{\max-nom} \Rightarrow [(D - 3d_2 + 2)k + D + 2d_1 + 2d_2 - 3] \times V_1/12f_sL \le 0.195kV_1/2f_sL. \tag{26}$$

To keep ZVS, the constraint of ZVS in PFTM is shown in (18). Combined with (19), (24), and (26), the optimal range of phase shift ratios D and $d_1 = d_2$ are obtained, as in Fig. 16(b).

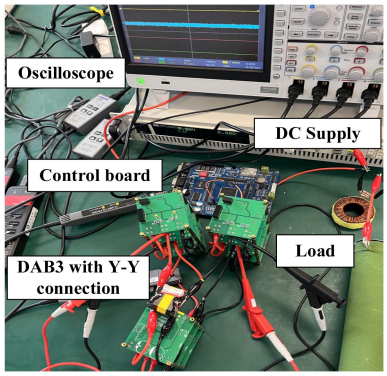

Fig. 17. Experimental setup.

TABLE IV
PARAMETERS OF DAB3 EXPERIMENTS SETUP

Parameters	Values	Parameters	Values
V_1	400 V	L	14 μH
V_2	250 V	fs	10 kHz
n	2:1	*Switches* 1–12	FDPF12N60NZ

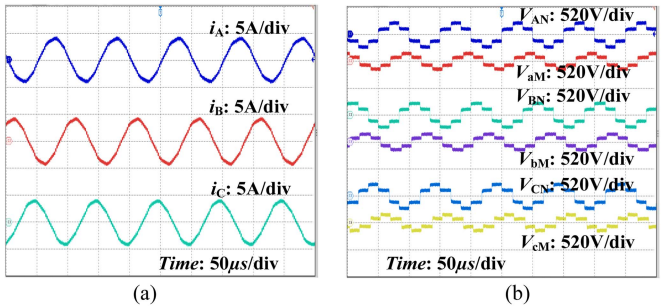

Fig. 18. Waveforms of HFL current and voltage in normal operation. (a) Three-phase currents. (b) Three-phase voltages.

Therefore, according to the transmission power range in Fig. 12 and phase shift ratio optimal range in Fig. 16, the phase shift ratios between fault phase and normal phase are optimized. The operation of normal switch in fault legs/paths is recon-figured, optimizing the duration of corresponding modalities about antiparallel diodes. Thus, under transmission power improvement in PFTM, HFL current stress is reduced and ZVS is kept during fault-tolerant operation of DAB3.

V. EXPERIMENTAL VERIFICATION

In this section, a DAB3 with the Y-Y connection experiments setup is established in Fig. 17, which contains a dc supply, control board, and oscilloscope based on Tektronix MSO56 and TBS 2000B. The main parameters are presented in Table IV. In normal operation in Fig. 18, i_A, i_B, and i_C are symmetric without dc bias, and the maximum value I_{max} is about 4 A.

A. Transmission Power From Primary Side to Secondary Side

To verify the effectiveness of PFTM, the comparison experiments of PFTM, open-phase method, and frozen-fault-leg method are completed, when SOCF in primary and secondary sides. The transmission power in these experiments is from primary side to secondary side, where the dc voltage source is on the primary side and the output load is on the secondary side.

The PFTM is employed when S_1 and S_7 are SOCF in Figs. 19 and 20, respectively. When S_1 is SOCF, in Fig. 19(a) and (b), a completely negative dc bias occurs in i_A and a positive dc bias occurs in i_B and i_C. The maximum value I_{max} is about 7.5 A, exceeding the normal current stress. In Fig. 19(d) and (e), the primary HFL voltages present the duty loss. During PFTM in Fig. 19(c), the negative dc bias of i_A and the positive dc bias of i_B and i_C are alleviated. I_{max} is decreased to 3.6 A, which reduces the current stress. Besides, the ZVS is achieved. In Fig. 19(f), the primary HFL voltages are returned to normal. When S_7 is SOCF, in Fig. 20(a) and (b), a positive dc bias occurs in i_A and a negative dc bias occurs in i_B and i_C. The maximum value I_{max} is about 6.2 A, exceeding the normal current stress. In Fig. 20(d) and (e), the secondary HFL voltages present the duty loss. During PFTM in Fig. 20(c), I_{max} is decreased to 3.2 A, and the current stress is reduced. Besides, the ZVS is achieved. In Fig. 20(f), the secondary HFL voltages are reshaped, and the duty loss is complemented.

The open-phase method is employed, when S_1 and S_7 are SOCF in Figs. 21 and 22, respectively. When S_1 is SOCF, in open-phase method in Fig. 21(a) and (b), the HFL current in fault phase A is zero, and HFL currents in phases B and C are shifted by T_{hs}. In Fig. 21(c) and (d), HFL voltages in fault A are zero, and HFL currents in phases B and C are two-level square waves and are shifted by T_{hs}. When S_7 is SOCF, in open-phase method in Fig. 22, the HFL currents and voltages are the same as that in Fig. 21.

The frozen-fault-leg method is employed, when S_1 and S_7 are SOCF in Figs. 23 and 24, respectively. When S_1 is SOCF, in frozen-fault-leg method, the S_1 and S_2 on the fault leg are frozen so that the rest of paths are not related to S_1 and S_2. Then, according to Table I, there is no feasible path that transfers the power from the primary side to the secondary side in fault phase A. Thus, in Fig. 23(a) and (b), there is only a small HFL current in fault phase A, and HFL currents in phases B and C are shifted by T_{hs}. Besides, excessive current stress occurs in the transition process. In Fig. 23(c) and (d), HFL voltages present the duty loss. When S_7 is SOCF, in frozen-fault-leg method in Fig. 24(a) and (b), the current stress in HFL is reduced. However, in Fig. 24(c) and (d), HFL voltages present the duty loss.

Besides, the input/output currents and voltages under PFTM and traditional methods, when S_1 and S_7 under SOCF are displayed in Fig. 25. When S_1 is SOCF, in PFTM, output voltage V_2 is dropped from 257 to 205.5 V, as in Fig. 25(a). In open-phase method, V_2 is dropped from 257 to 171.4 V, as in Fig. 25(b). In frozen-fault-leg method, V_2 is dropped from 257 to 126.5 V, as in Fig. 25(c). When S_7 is SOCF, in PFTM, V_2 is dropped from 257 to 205 V, as in Fig. 25(d). In open-phase method, V_2 is dropped from 257 to 171.4 V, as in Fig. 25(e). In frozen-fault-leg method, V_2 is dropped from 257 to 187 V, as in Fig. 25(f). Therefore, When SOCF occurs on primary side, the transmission power from fault primary side to normal secondary side is enhanced in PFTM. When SOCF occurs on secondary

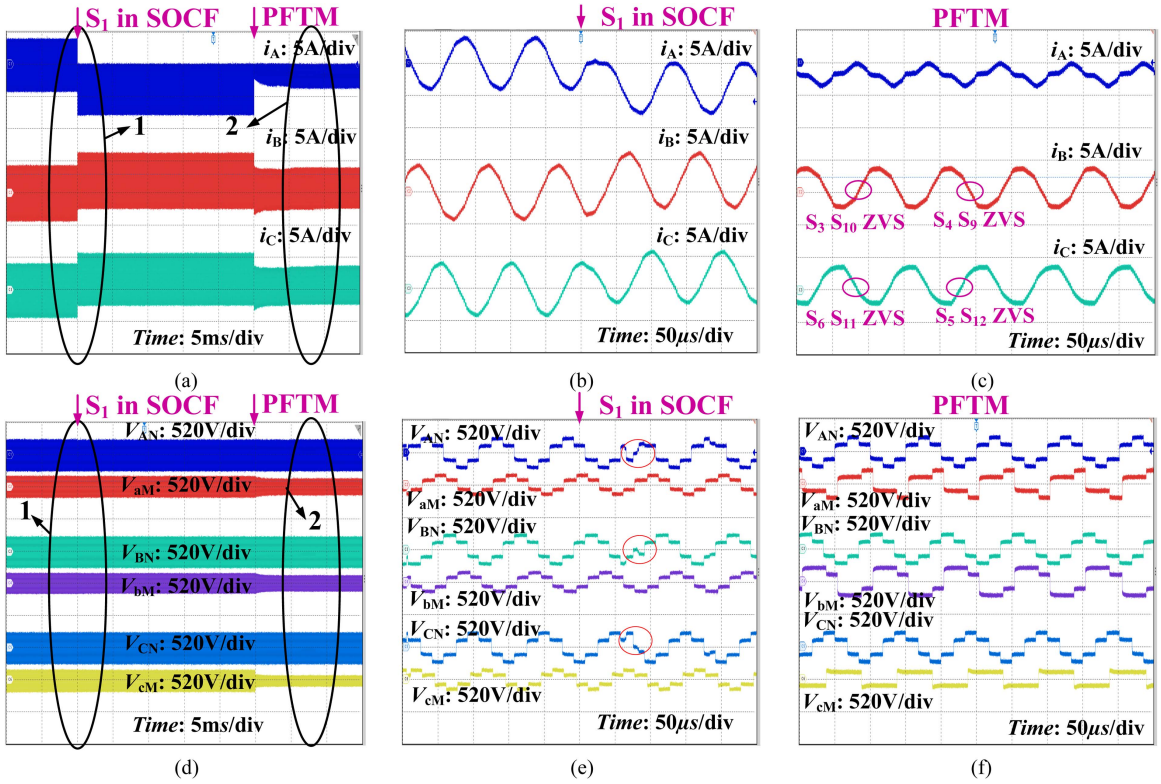

Fig. 19. HFL currents and voltages in PFTM, when S_1 is SOCF. (a) HFL currents. (b) Region 1 of HFL currents, zoom-in view. (c) Region 2 of HFL currents, zoom-in view. (d) HFL voltages. (e) Region 1 of HFL voltages, zoom-in view. (f) Region 2 of HFL voltages, zoom-in view.

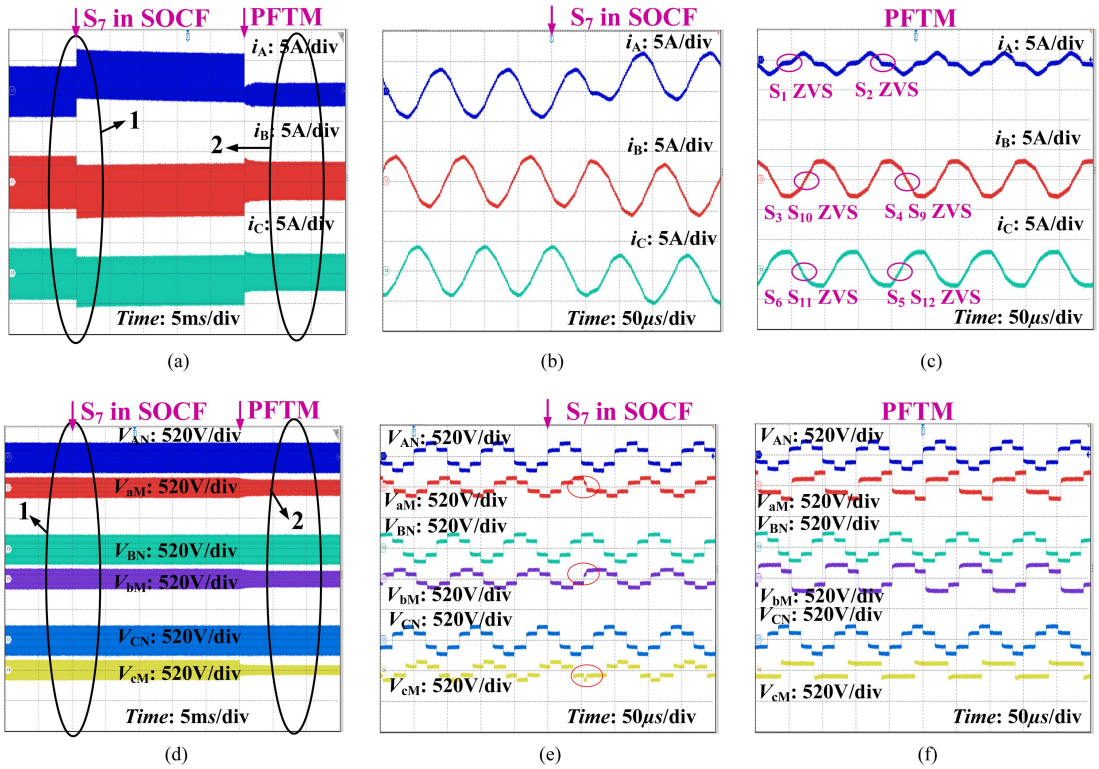

Fig. 20. HFL currents and voltages in PFTM, when S_7 is SOCF. (a) HFL currents. (b) Region 1 of HFL currents, zoom-in view. (c) Region 2 of HFL currents, zoom-in view. (d) HFL voltages. (e) Region 1 of HFL voltages, zoom-in view. (f) Region 2 of HFL voltages, zoom-in view.

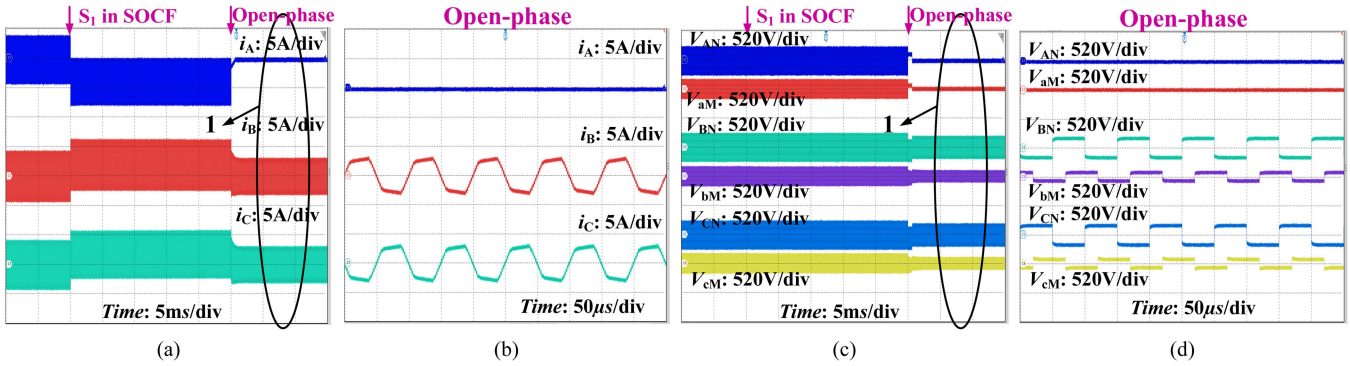

Fig. 21. HFL currents and voltages in open-phase method, when S_1 is SOCF. (a) HFL currents. (b) Zoom-in view of (a). (c) HFL voltages. (d) Zoom-in view of (c).

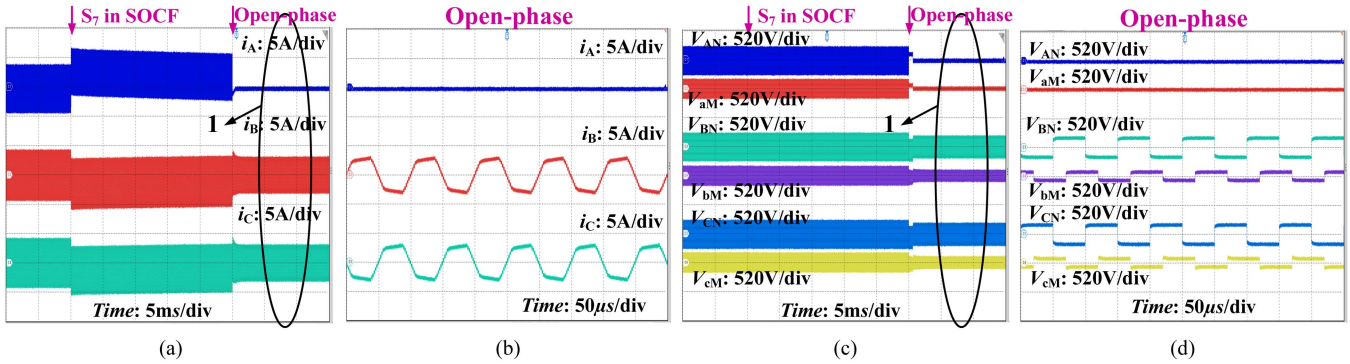

Fig. 22. HFL currents and voltages in open-phase method, when S_7 is SOCF. (a) HFL currents. (b) Zoom-in view of (a). (c) HFL voltages. (d) Zoom-in view of (c).

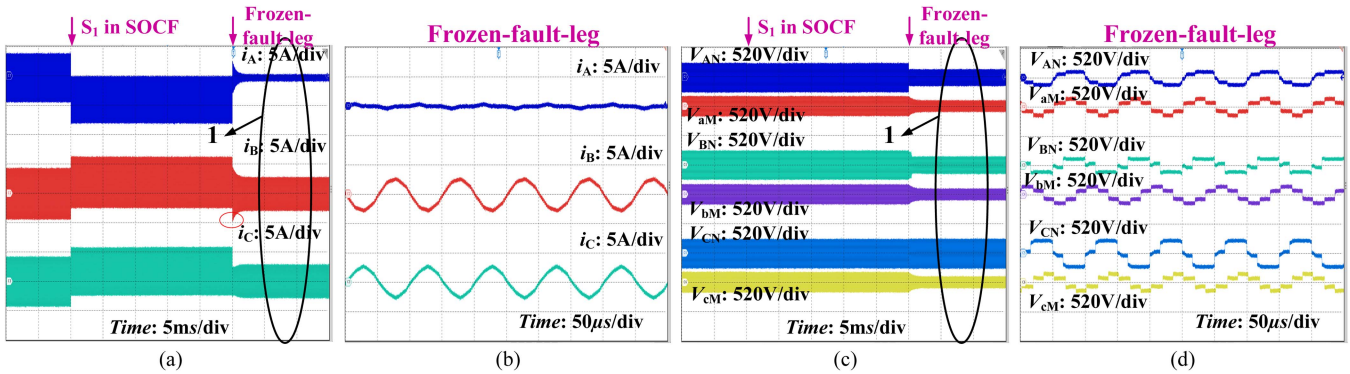

Fig. 23. HFL currents and voltages in frozen-fault-leg method, when S_1 is SOCF. (a) HFL currents. (b) Zoom-in view of (a). (c) HFL voltages. (d) Zoom-in view of (c).

side, the transmission power from normal primary side to fault secondary side is enhanced in PFTM.

B. Transmission Power From Secondary Side to Primary Side

To prove the bidirectional power transfer capability in PFTM, the experiments about transmission power from secondary side to primary side are also shown in Figs. 26–28. The output load of secondary side is replaced by a dc voltage source, where the voltage is set as 250 V. The dc voltage source of primary side is replaced by a load, where the voltage is set as about 400 V.

Under load in primary side in Fig. 26(a) and (b), when PFTM is employed for S_1 in SOCF, positive dc bias of i_A and the negative dc bias of i_B and i_C are alleviated. I_{max} is decreased from 7.8 to 3.6 A, which reduces the current stress. Besides, in Fig. 26(c) and (d), the HFL voltages are returned to normal. Moreover, in Fig. 28(a), the output voltage V_1 of primary side is dropped from 402 to 320.6 V in PFTM, which is 79.7% of the

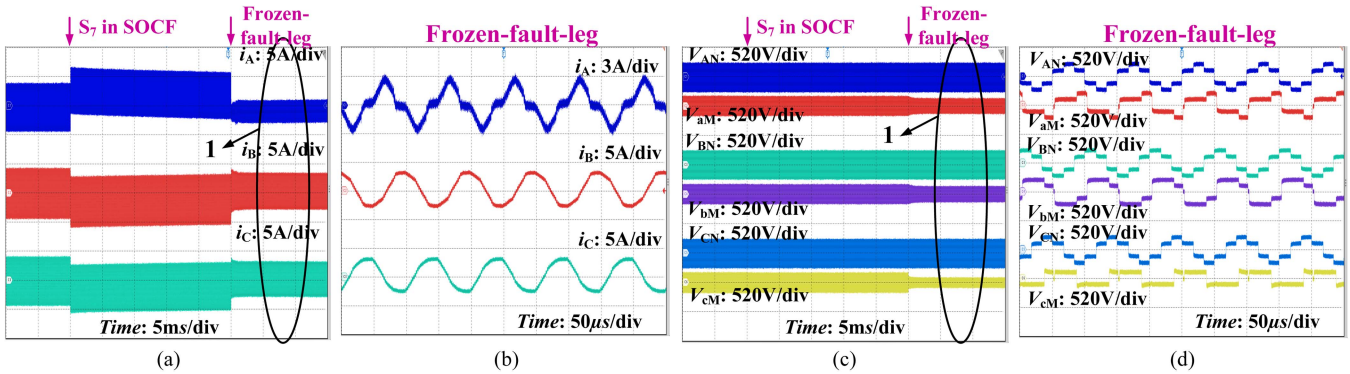

Fig. 24. HFL currents and voltages in frozen-fault-leg method, when S_7 is SOCF. (a) HFL currents. (b) Zoom-in view of (a). (c) HFL voltages. (d) Zoom-in view of (c).

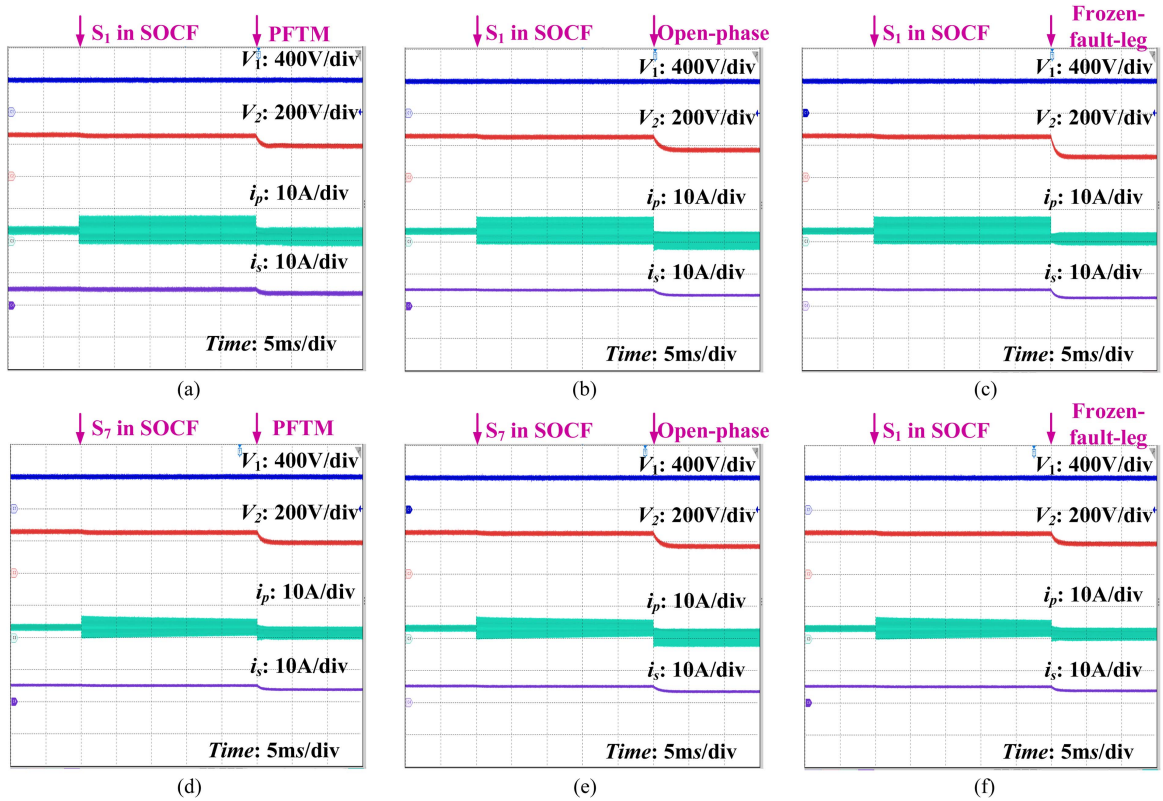

Fig. 25. Input/output currents and voltages in SOCF. (a) PFTM, when S_1 is SOCF. (b) Open-phase method, when S_1 is SOCF. (c) Frozen-fault-leg method, when S_1 is SOCF. (d) PFTM, when S_7 is SOCF. (e) Open-phase method, when S_7 is SOCF. (f) Frozen-fault-leg method, when S_7 is SOCF.

normal. Thus, the experiment results and operation characteristics in Figs. 26(a), (b), and 28(a) are consistent with PFTM for secondary side SOCF under load in secondary side in Figs. 20 and 25(d).

Under load in primary side in Fig. 27(a) and (b), when PFTM is employed for S_7 in SOCF, negative dc bias of i_A and the positive dc bias of i_B and i_C are alleviated. I_{max} is decreased from 9.6 to 5.0 A, which reduces the current stress. Besides, in Fig. 27(c) and (d), the HFL voltages are returned to normal. Moreover, in Fig. 28(b), the output voltage V_1 of primary side is dropped from 402 to 321.9 V in PFTM, which is 80% of the normal. Thus, the experiment results and operation characteristics in Figs. 27(a), (b), and 28(b) are consistent with PFTM for primary side SOCF under load in secondary side in Figs. 19 and 25(a).

C. PFTM Under Various Conditions

To prove the effectiveness of PFTM under the various conditions, the experiments of PFTM under load variation are shown in Figs. 29, 30, and the experiments of PFTM under D, d_1, d_2, k gains variation are shown in Figs. 31–33.

1) Load Variation: To explore the influence of varied loads on the PFTM, the currents and voltages in PFTM are shown in Figs. 29 and 30, when R in the load is reduced from 5 Ω to 3.5 Ω.

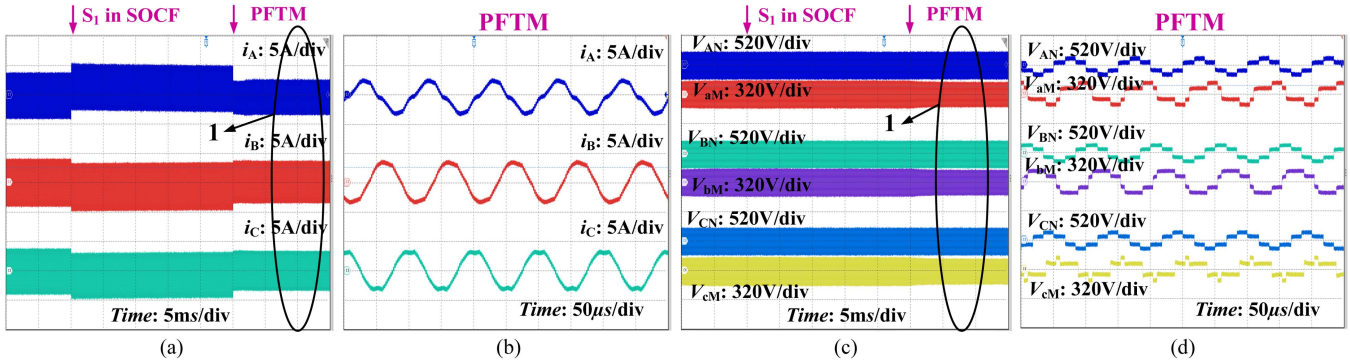

Fig. 26. HFL currents and voltages in PFTM, when S_1 is SOCF. (a) HFL currents. (b) Zoom-in view of (a). (c) HFL voltages. (d) Zoom-in view of (c).

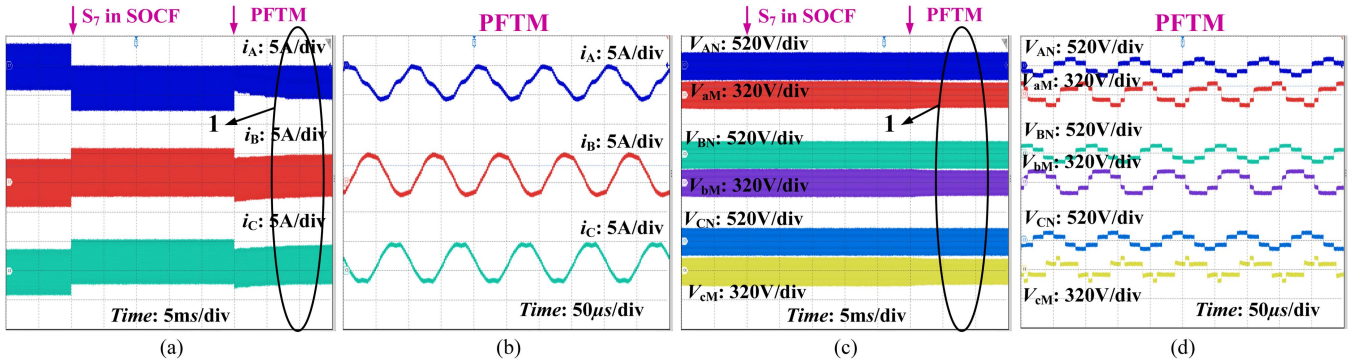

Fig. 27. HFL currents and voltages in PFTM, when S_7 is SOCF. (a) HFL currents. (b) Zoom-in view of (a). (c) HFL voltages. (d) Zoom-in view of (c).

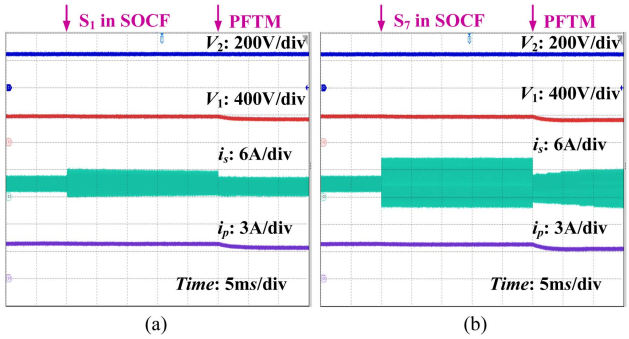

Fig. 28. Input/output currents and voltages in PFTM. (a) When S_1 is SOCF. (b) When S_7 is SOCF.

From Figs. 29(a) and (b), when the PFTM is employed for S_1 in SOCF, there is almost no fluctuation in the HFL current and voltage waveforms under load variation. Besides, in Fig. 29(c), the output current is from 3.7 to 3.9 A, and the output voltage is from 205.5 to 200 V, which is stable under load variation. From Fig. 30(a) and (b), when the PFTM is employed for S_7 in SOCF, there is almost no fluctuation in the HFL current and voltage waveforms under load variation. Besides, in Fig. 30(c), the output current is from 3.7 to 3.9 A, and the output voltage is from 205.5 to 200 V, which is stable under load variation.

Therefore, the PFTM has good stability under load variation, when SOCF is in primary and secondary sides.

2) D, d_1, d_2, and k Gains Variation: To explore the influences of varied D, d_1, d_2, and k on the PFTM, the currents and voltages in PFTM are shown in Figs. 31–33, when $D = 0.25$, $d_1 = 0.7$, $d_2 = 0.7$, and voltage gain $k = 0.7$.

In Fig. 31(a) and (b), when PFTM is employed for S_1 in SOCF, the negative dc bias of i_A and the positive dc bias of i_B and i_C are alleviated. I_{max} is decreased from 6.1 to 2.8 A, which reduces the current stress. Besides, in Fig. 31(c) and (d), the primary HFL voltages are returned to normal. Moreover, in Fig. 33(a), the output voltage V_2 is dropped from 137 to 110 V in PFTM, which is 80.2% of the normal.

In Fig. 32(a) and (b), when PFTM is employed for S_7 in SOCF, the positive dc bias of i_A and the negative dc bias of i_B and i_C are alleviated. I_{max} is decreased from 5.8 to 2.8 A, which reduces the current stress. Besides, in Fig. 32(c) and (d), the secondary HFL voltages are returned to normal. Moreover, in Fig. 33(b), the output voltage V_2 is dropped from 143 to 114 V in PFTM, which is 79.7% of the normal.

Therefore, the fault-tolerant operation is also achieved in PFTM, when D, d_1, d_2, and k are varied.

D. PFTM for Tolerance of Double SOCFs in the Same Side and in Both Sides

In addition to the application of PFTM when single SOCF occurs on primary side and secondary side, the applications of PFTM in double SOCFs in the same side and in both

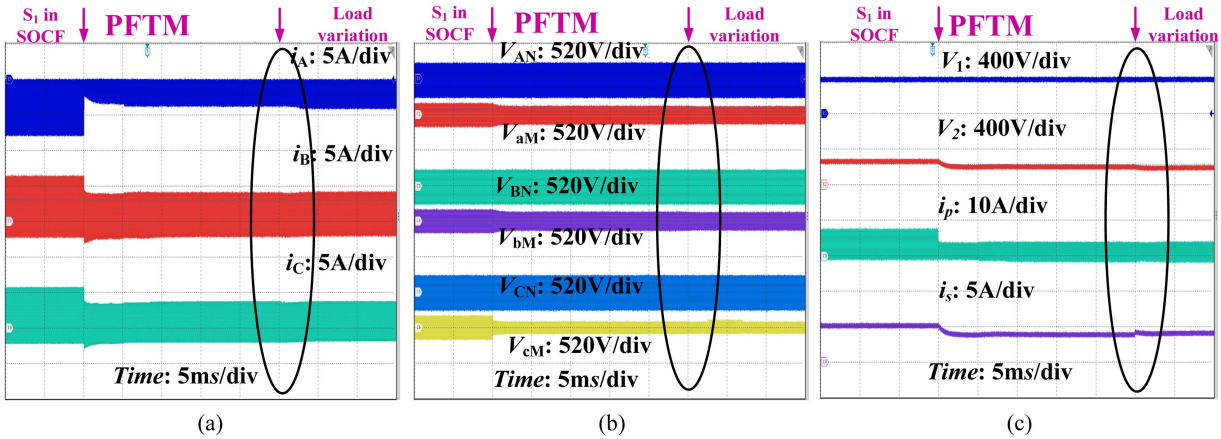

Fig. 29. Currents and voltages in PFTM under load variation, when S_1 is SOCF. (a) HFL currents. (b) HFL voltages. (c) Input/output currents and voltages.

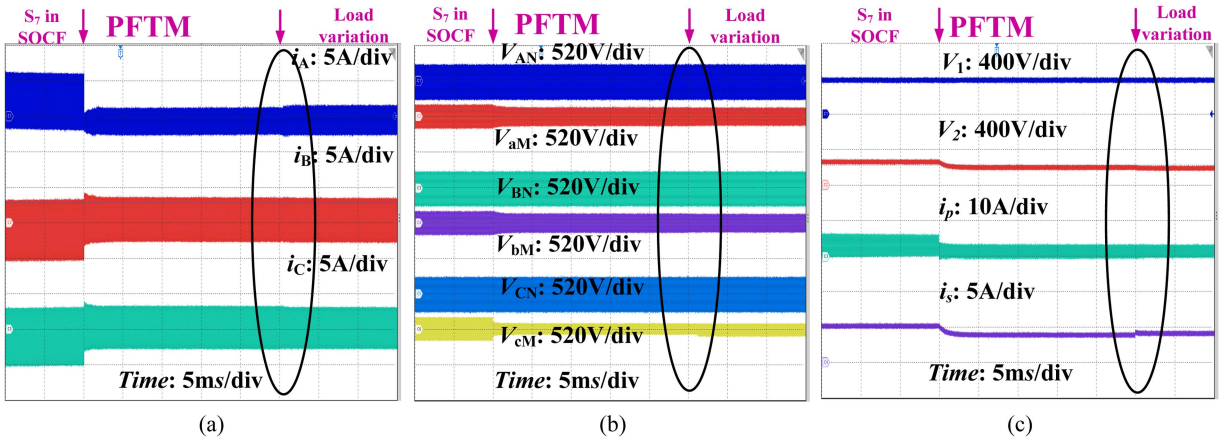

Fig. 30. Currents and voltages in PFTM under load variation, when S_7 is SOCF. (a) HFL currents. (b) HFL voltages. (c) Input/output currents and voltages.

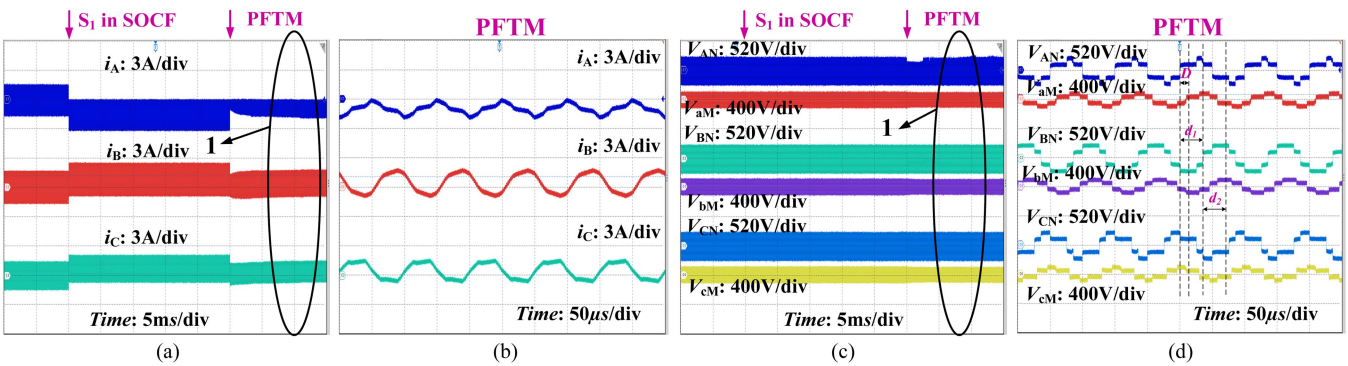

Fig. 31. HFL currents and voltages in PFTM under D, d_1, d_2, and k variation, when S_1 is SOCF. (a) HFL currents. (b) Zoom-in view of (a). (c) HFL voltages. (d) Zoom-in view of (c).

sides are shown in Figs. 34–40, which contains the following categories.

1) Double SOCFs in the Same Side of the Same Phase: PFTM is employed under both S_1 and S_2 in SOCF, as shown in Fig. 34. In this situation, fault tolerance can be achieved. The result in PFTM is similar to the result in open-phase without adjusting phase differences, and the output voltage is decreased from 257 to 135.2 V.

PFTM is employed under both S_7 and S_8 in SOCF, as in Fig. 35. In this situation, fault tolerance can be achieved. The

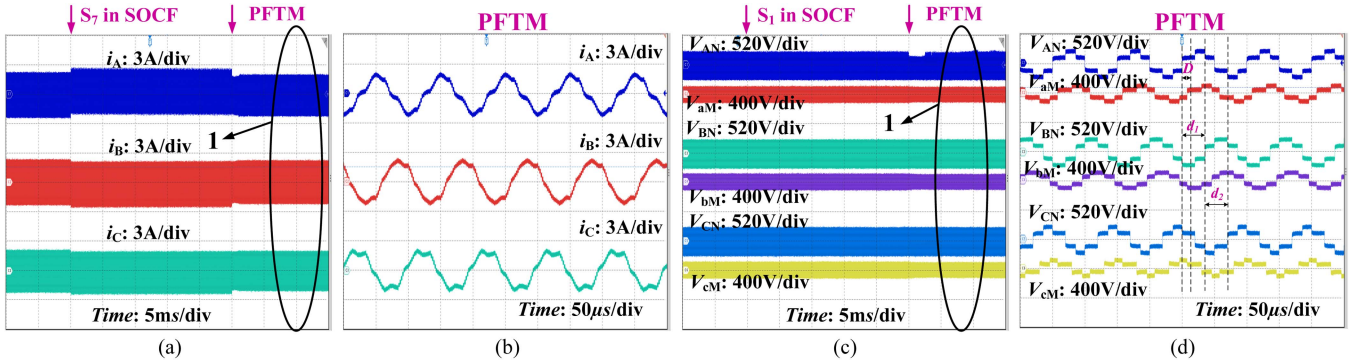

Fig. 32. HFL currents and voltages in PFTM under D, d_1, d_2, and k variation, when S_7 is SOCF. (a) HFL currents. (b) Zoom-in view of (a). (c) HFL voltages. (d) Zoom-in view of (c).

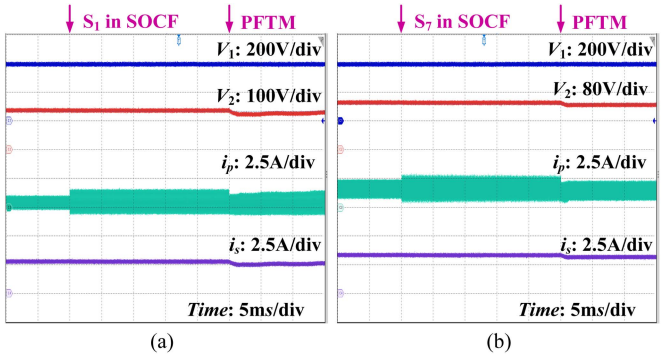

Fig. 33. Input/output currents and voltages in PFTM under D, d_1, d_2, and k variation. (a) When S_1 is SOCF. (b) When S_7 is SOCF.

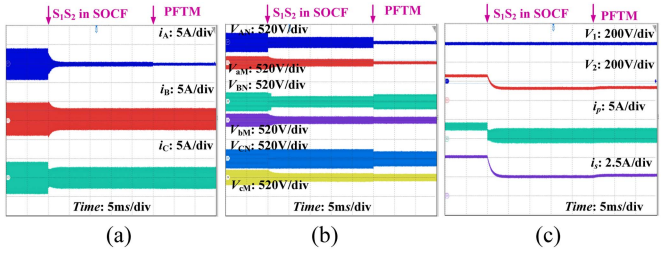

Fig. 34. Currents and voltages in PFTM, when S_1 and S_2 are SOCF. (a) HFL currents. (b) HFL voltages. (c) Input/output currents and voltages.

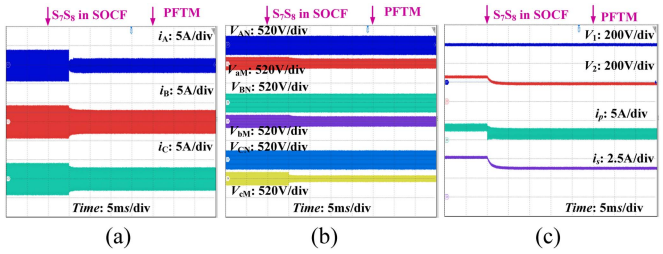

Fig. 35. Currents and voltages in PFTM, when S_7 and S_8 are SOCF. (a) HFL currents. (b) HFL voltages. (c) Input/output currents and voltages.

result is consistent with PFTM employed when S_7 is SOCF, and the output voltage is decreased from 257 to 203 V.

2) Double SOCFs in Both Sides of the Same Phase: PFTM is employed under both S_1 and S_8 in SOCF, as in Fig. 36. In this

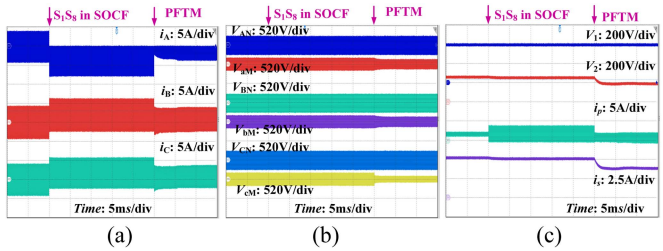

Fig. 36. Currents and voltages in PFTM, when S_1 and S_8 are SOCF. (a) HFL currents. (b) HFL voltages. (c) Input/output currents and voltages.

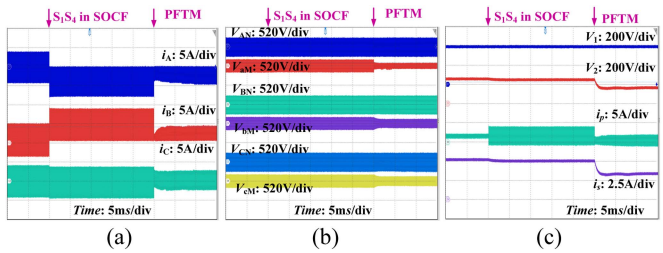

Fig. 37. Currents and voltages in PFTM, when S_1 and S_4 are SOCF. (a) HFL currents. (b) HFL voltages. (c) Input/output currents and voltages.

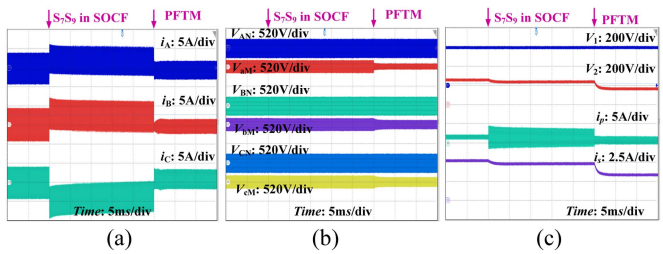

Fig. 38. Currents and voltages in PFTM, when S_7 and S_9 are SOCF. (a) HFL currents. (b) HFL voltages. (c) Input/output currents and voltages.

situation, fault tolerance can be achieved. The result is consistent with PFTM employed when S_1 is SOCF, and the output voltage is decreased from 257 to 205.5 V.

3) Double SOCFs in the Same Side of the Different Phases: PFTM is employed under both S_1 and S_4 in SOCF, as in Fig. 37. In this situation, fault tolerance can be achieved, and the output voltage is decreased from 257 to 167 V.

TABLE V
COMPARISONS OF EXPERIMENTAL OUTCOMES IN PFTM, OPEN-PHASE METHOD, AND FROZEN-FAULT-LEG METHOD

Fault-tolerant method	SOCF on the primary side					SOCF on the secondary side				
	V_2(V)	I_{max}(A)	P/P_{nom}	ZVS	Bidirectional	V_2(V)	I_{max}(A)	P/P_{nom}	ZVS	Bidirectional
PFTM	205.5	3.6	80.5%	√	√	205	3.2	80.5%	√	√
Open-phase [21]	171.4	3.6	66.7%	√	√	171.4	3.6	66.7%	√	√
Frozen-fault-leg [17]	126.5	3.5	51%	√	×	187	3.7	72.7%	√	×

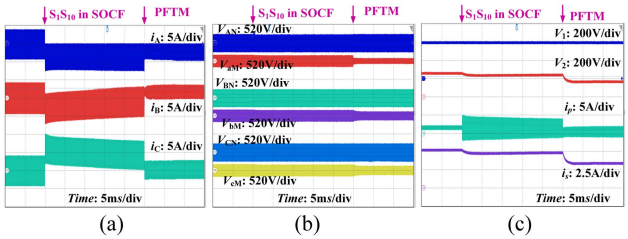

Fig. 39. Currents and voltages in PFTM, when S_1 and S_{10} are SOCF. (a) HFL currents. (b) HFL voltages. (c) Input/output currents and voltages.

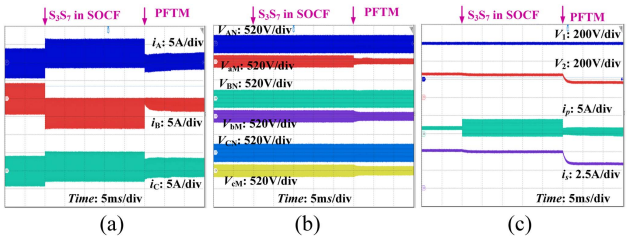

Fig. 40. Currents and voltages in PFTM, when S_3 and S_7 are SOCF. (a) HFL currents. (b) HFL voltages. (c) Input/output currents and voltages.

PFTM is employed under both S_7 and S_9 in SOCF, as in Fig. 38. In this situation, fault tolerance can be achieved, and the output voltage is decreased from 257 to 164 V.

4) Double SOCFs in Both Sides of the Different Phases: PFTM is employed under both S_1 and S_{10} in SOCF, as in Fig. 39. In this situation, fault tolerance can be achieved, and the output voltage is decreased from 257 to 166 V.

PFTM is employed under both S_3 and S_7 in SOCF, as in Fig. 40. In this situation, fault tolerance can be achieved, and the output voltage is decreased from 257 to 165 V.

In general, the fault tolerance of double SOCFs can also be achieved by PFTM, when the double SOCFs occur in the same side and in both sides. Compared with the single SOCF tolerance, the PFTM can maintain HFL current stress under the maximum HFL current in normal, however, leading to a heavy drop in transmission power and voltage. It is because the current path is lost greatly in double SOCFs. Thus, the proposed PFTM in this article is mainly for the single SOCF tolerance. The fault-tolerant method for double SOCFs is further investigated in future work.

E. Comparisons in PFTM, Open-Phase Method, and Frozen-Fault-Leg Method

The experimental outcomes in PFTM, open-phase method, and frozen-fault-leg method are compared and listed in Table V. When SOCF occurs on primary side, compared with open-phase method and frozen-fault-leg method, the proposed PFTM can achieve a higher output voltage (205.5 V), a lower current stress (3.6 A), a larger transmission power (80.5%), and better bidirectional transmission power capability. Besides, ZVS is achieved by all fault-tolerant methods. When SOCF occurs on secondary side, compared with open-phase method and frozen-fault-leg method, the proposed PFTM can achieve a higher output voltage (205 V), a lower current stress (3.2 A), a larger transmission power (80.5%), and better bidirectional transmission power capability. Besides, ZVS is achieved by all fault-tolerant methods.

VI. CONCLUSION

In this article, a PFTM of DAB3 is proposed for SOCF in primary and secondary side bridges, improving bidirectional power transmission and reducing current stress based on fault-tolerant operation. The transferred energy of each phase is investigated by modality and path analysis, then, a path energization method is proposed to introduce PFTM, and the switching pattern reconfiguration strategy is summarized by switching functions during SOCF, enlarging the maximum transmission power within maximum HFL inductor current. Moreover, PFTM is proposed for SOCF tolerance on primary and secondary sides. In the PFTM, the fault paths/legs are employed, reconfiguring the current path of modality, actively adjusting the ON-time of antiparallel diode, and realizing the bidirectional transmission power improvement. Furthermore, the optimization strategy of phase shift ratio is proposed, to reduce HFL current stress and keep ZVS. Compared with traditional methods, in PFTM, power range, and voltage gain are increased by 24% and 20%, respectively. Moreover, the idea of reconstructing fault paths and path energization can be applied to the fault tolerance of other multiswitch converters.

REFERENCES

[1] D. Sera, M. Kerekes, T. K. Sen, and P. Rodriguez, "DC microgrids—Part I: A review of control strategies and stabilization techniques," *IEEE Trans. Power Electron.*, vol. 31, no. 5, pp. 3524–3541, May 2016.

[2] R. W. A. A. De Doncker, D. M. Divan, and M. H. Kheraluwala, "A three-phase soft-switched high-power-density DC/DC converter for high-power applications," *IEEE Trans. Ind. Appl.*, vol. 27, no. 1, pp. 63–73, Jan./Feb. 1991.

[3] L. F. Costa, F. Hoffmann, G. Buticchi, and M. Liserre, "Comparative analysis of multiple active bridge converters configurations in modular smart transformer," *IEEE Trans. Ind. Electron.*, vol. 66, no. 1, pp. 191–202, Jan. 2019.

[4] S. Siouane, S. Jovanović, and P. Poure, "Open-switch fault-tolerant operation of a two-stage buck/buck-boost converter with redundant synchronous switch for PV systems," *IEEE Trans. Ind. Electron.*, vol. 66, no. 5, pp. 3938–3947, May 2019.

[5] L. F. Costa and M. Liserre, "Failure analysis of the DC–DC converter: A comprehensive survey of faults and solutions for improving reliability," *IEEE Power Electron. Mag.*, vol. 5, no. 4, pp. 42–51, Dec. 2018.
[6] S. K. Rastogi, S. S. Shah, B. N. Singh, and S. Bhattacharya, "Mode analysis, transformer saturation, and fault diagnosis technique for an open-circuit fault in a three-phase DAB converter," *IEEE Trans. Power Electron.*, vol. 38, no. 6, pp. 7644–7660, Jun. 2023.
[7] H. S. H. Wang, F. Blaabjerg, and M. Pecht, *Reliability of Power Electronic Converter Systems*. London, U.K.: IET, 2015.
[8] Y. Wang et al., "A multiple modular isolated DC/DC converter with bidirectional fault handling and efficient energy conversion for DC distribution network," *IEEE Trans. Power Electron.*, vol. 35, no. 11, pp. 11502–11517, Nov. 2020.
[9] D. Zhou, S. Yang, and Y. Tang, "A voltage-based open-circuit fault detection and isolation approach for modular multilevel converters with model-predictive control," *IEEE Trans. Power Electron.*, vol. 33, no. 11, pp. 9866–9874, Nov. 2018.
[10] L. Costa, G. Buticchi, and M. Liserre, "A fault-tolerant series-resonant DC–DC converter," *IEEE Trans. Power Electron.*, vol. 32, no. 2, pp. 900–905, Feb. 2017.
[11] X. Jiang, Q. Li, W. Huang, and R. Cao, "A dual-winding fault-tolerant motor drive system based on the redundancy bridge arm," *IEEE Trans. Ind. Electron.*, vol. 66, no. 1, pp. 654–662, Jan. 2019.
[12] S. Xu, J. Zhang, and J. Hang, "Investigation of a fault-tolerant three-level T-type inverter system," *IEEE Trans. Ind. Appl.*, vol. 53, no. 5, pp. 4613–4623, Sep./Oct. 2017.
[13] P. S. Bhakar and K. Jayaraman, "A new fault-tolerant scheme for switch failures in dual active bridge DC–DC converter," *IEEE J. Emerg. Sel. Topics Power Electron.*, vol. 10, no. 6, pp. 7627–7637, Dec. 2022.
[14] H. Shi, H. Wen, G. Chen, Q. Bu, G. Chu, and Y. Zhu, "Multiple-fault-tolerant dual active bridge converter for DC distribution system," *IEEE Trans. Power Electron.*, vol. 37, no. 2, pp. 1748–1760, Feb. 2022.
[15] Y. Wang, Y. Guan, M. Molinas, O. B. Fosso, W. Hu, and Y. Zhang, "Open-circuit switching fault analysis and tolerant strategy for dual-active-bridge DC–DC converter considering parasitic parameters," *IEEE Trans. Power Electron.*, vol. 37, no. 12, pp. 15020–15034, Dec. 2022.
[16] C. Song, A. Sangwongwanich, Y. Yang, and F. Blaabjerg, "Open-circuit fault diagnosis and tolerant control for 2/3-level DAB converters," *IEEE Trans. Power Electron.*, vol. 38, no. 4, pp. 5392–5410, Apr. 2023.
[17] S. Haghbin, F. Blaabjerg, and A. S. Bahman, "Frozen leg operation of a three-phase dual active bridge converter," *IEEE Trans. Power Electron.*, vol. 34, no. 5, pp. 4239–4248, May 2019.
[18] N. Zhao, J. Liu, Y. Shi, J. Yang, J. Zhang, and X. You, "Mode analysis and fault-tolerant method of open-circuit fault for a dual active-bridge DC–DC converter," *IEEE Trans. Ind. Electron.*, vol. 67, no. 8, pp. 6916–6926, Aug. 2020.
[19] H. Wen, J. Li, H. Shi, Y. Hu, and Y. Yang, "Fault diagnosis and tolerant control of dual-active-bridge converter with triple-phase shift control for bidirectional EV charging systems," *IEEE Trans. Transp. Electrific.*, vol. 7, no. 1, pp. 287–303, Mar. 2021.
[20] M. Berger, I. Kocar, H. Fortin-Blanchette, and C. Lavertu, "Open-phase fault-tolerant operation of the three-phase dual active bridge converter," *IEEE Trans. Power Electron.*, vol. 35, no. 4, pp. 3651–3662, Apr. 2020.
[21] T.-T. Le, M.-K. Nguyen, T.-D. Duong, C. Wang, and S. Choi, "Open-circuit fault-tolerant control for a three-phase current-fed dual active bridge DC–DC converter," *IEEE Trans. Ind. Electron.*, vol. 70, no. 2, pp. 1586–1596, Feb. 2023.
[22] N. H. Baars, J. Everts, C. G. E. Wijnands, and E. A. Lomonova, "Performance evaluation of a three-phase dual active bridge DC–DC converter with different transformer winding configurations," *IEEE Trans. Power Electron.*, vol. 31, no. 10, pp. 6814–6823, Oct. 2016.
[23] J. E. Ochoa Sosa, R. O. Núñez, G. G. Oggier, and G. O. García, "Open transistors fault-tolerant schemes of three-phase dual active bridge DC–DC converters," *IEEE Latin Amer. Trans.*, vol. 19, no. 3, pp. 385–395, Mar. 2021.
[24] D. Mou et al., "A periodic-steady-state analysis model in time domain for dual active bridge converter," *IEEE Trans. Power Electron.*, vol. 37, no. 4, pp. 4121–4132, Apr. 2022.

Yuanpeng Guan received the B.S. degree in electrical engineering from the Huazhong University of Science and Technology, Wuhan, China, in 2014, the M.S. degree in power electronic from South China University of Technology, Guangzhou, China, in 2017, and the Ph.D. degree in power electronic from the School of Electric Power, South China University of Technology, Guangzhou, China, in 2020.

From 2020 to 2023, he was an Associate Professor with the Energy Electricity Research Center, International Energy College, Jinan University, Zhuhai, China. He is currently an Associate Professor with the School of Automation, Guangdong University of Technology, Guangzhou, China. His current research interests include grid-connected inverter and dual-active-bridge dc–dc converter.

Yiting Xiao received the B.S. degree in information security in 2021 from Jinan University, Zhuhai, China, where she is currently working toward the M.S. degree in circuit and system with Energy Electricity Research Center.

Her current research interests include dual-active-bridge dc–dc converter and open circuit fault tolerance.

Li Qin received the B.Sc. and M.Sc. degrees in electrical engineering from the South China University of Technology, Guangzhou, China, in 2013 and 2017, respectively. He is currently working toward the Ph.D. degree in power electronics with Guangxi University, Nanning, China.

He joined Foshan Power Supply Bureau of Guangdong Power Grid Company, Ltd., and China Energy Engineering Group Guangxi Electric Power Design and Research Institute Company, Ltd., in 2017 and 2019, respectively. His current research interests include modular multilevel converter and dual-active-bridge dc–dc converter.

Xiong Liu (Senior Member, IEEE) received the B.E. and M.Sc. degrees in electrical engineering from the Huazhong University of Science and Technology, Wuhan, China, in 2006 and 2008, respectively, and the Ph.D. degree in electrical engineering from the School of Electrical and Electronic Engineering, Nanyang Technological University, Singapore, in 2013.

From July to November 2008, he was an Engineer with Shenzhen Nanrui Technologies Company, Ltd., Shenzhen, China. From 2011 to 2012, he was a Visiting Scholar with the Department of Energy Technology, Aalborg University, Aalborg East, Denmark. From 2012 to 2013, he was a Researcher with the Energy Research Institute, Nanyang Technological University. From 2013 to 2020, he was a Principal Technologist with Rolls-Royce Electrical, Rolls-Royce Singapore Pte. Ltd., Singapore. He is currently an Associate Professor with the Energy Electricity Research Center, International Energy College, Jinan University, Zhuhai, China. His research interests include power electronics, motor drive, and electrical/hybrid propulsion system for marine and aerospace.

Dr. Liu was the recipient of the Best Paper Award at the IEEE International Power Electronics and Motion Control Conference-Energy Conversion Congress and Exposition Asia in 2012.

Hui Deng received the M.Sc. and Ph.D. degrees in control engineering from North China Electric Power University, Beijing, China, in 2007 and 2016, respectively.

From 2016 to 2019, he was a Postdoctoral Fellow with the School of Control and Computer Engineering, North China Electric Power University, Beijing, China. He joined the Faculty of the Energy Electricity Research Center, Jinan University, Zhuhai, China, where he is currently an Associate Professor. His research interests include intelligent systems and process control.

Weixiong Wu received the B.S. degree in thermal energy and power engineering from the Guangdong University of Technology, Guangzhou, China, in 2012, the M.S. degree in thermal energy and power engineering from the Guangdong University of Technology, Guangzhou, China, in 2015, and the Ph.D. degree in energy chemical engineering from South China University of Technology, Guangzhou, China, in 2019.

He is currently an Associate Professor with the Energy Electricity Research Center, International Energy College, Jinan University, Zhuhai, China. His current research focuses on the engineering thermophysics involved problems in new energy utilization and energy storage, such as battery management and integrated optimization of energy storage system.